11/13/03

Global Changes of the Water Cycle Intensity

Michael G. Bosilovich *
Siegfried D. Schubert
And Gregory K. Walker

NASA Global Modeling and Assimilation Office
Code 900.3 Goddard Space Flight Center
Greenbelt MD

Submitted to J. Climate

---

* *Corresponding address*: Global Modeling and Assimilation Office, Code 900.3, NASA Goddard Space Flight Center, Greenbelt, MD 20771, Michael.Bosilovich@nasa.gov

Popular Summary of "Global Changes of the Water Cycle Intensity" by Michael G. Bosilovich, Siegfried D. Schubert and Gregory K. Walker

The water cycle of the Earth is defined by the evaporation of water from the surface to the atmosphere and then by the precipitation from the atmosphere back to the surface. A crucial question, considering that the climate of the Earth is changing, is how will the water cycle change. In this study, we evaluate atmospheric numerical simulations of the twentieth century climate, focusing on the changes of the global water cycle. A new diagnostic, using fewer simplifications than conventional methods, of atmospheric water vapor cycling rate is developed and employed. This diagnostic is compared to a simplified traditional calculation of cycling rate, based on monthly averages of precipitation and total water content. The mean sensitivity of both diagnostics to variations in climate forcing is comparable. However, the new diagnostic produces systematically larger values and more variability than the conventional average approach.

Climate simulations were performed using SSTs of the early (1902-1921) and late (1979-1998) twentieth century along with the appropriate CO2 forcing. In general, the increase of global precipitation with the increases in SST that occurred between the early and late twentieth century is small. However, an increase of atmospheric temperature leads to a systematic increase in total water in the air. As a result, the amount of time water spends in the atmosphere increased, indicating a smaller global cycling rate. This result was explored further using a number of 50-year simulations from different models forced with the same observed SST (1949-1998). The anomalies and trends in the water cycling rate and hydrologic variables of different GCMs are remarkably similar. The global annual precipitation shows a significant upward trend related to the upward trend of surface temperature, especially during the latter quarter of the twentieth century. While this implies an increase in the hydrologic cycle intensity, a concomitant increase of total precipitable water again leads to a decrease in the calculated global cycling rate. An analysis of the land/sea differences shows that the simulated precipitation over land has a decreasing trend while the oceanic precipitation has an increasing trend consistent with previous studies and the available observations. The decreasing continental trend in precipitation is located primarily over tropical land regions, with some other regions, such as North America experiencing an increasing trend. Further diagnostic tests are used to calculate the amount of precipitation recycling over land (namely, how much water from the land becomes precipitation over land). These diagnostics show that over global land areas, the recycling of continental moisture is decreasing in time. However, the recycling changes are not spatially uniform so that some regions, most notably over the United States, experience continental recycling of water that increases in time. While these results provide some new insight into the global water cycle, additional effort is needed to better define and understand the regional change in the water cycle.

Global Changes of the Water Cycle Intensity

ABSTRACT

In this study, we evaluate numerical simulations of the twentieth century climate, focusing on the changes in the intensity of the global water cycle. A new diagnostic of atmospheric water vapor cycling rate is developed and employed, that relies on constituent tracers predicted at the model time step. This diagnostic is compared to a simplified traditional calculation of cycling rate, based on monthly averages of precipitation and total water content. The mean sensitivity of both diagnostics to variations in climate forcing is comparable. However, the new diagnostic produces systematically larger values and more variability than the traditional average approach.

Climate simulations were performed using SSTs of the early (1902-1921) and late (1979-1998) twentieth century along with the appropriate CO2 forcing. In general, the increase of global precipitation with the increases in SST that occurred between the early and late twentieth century is small. However, an increase of atmospheric temperature leads to a systematic increase in total precipitable water. As a result, the residence time of water in the atmosphere increased, indicating a reduction of the global cycling rate. This result was explored further using a number of 50-year climate simulations from different models forced with observed SST. The anomalies and trends in the cycling rate and hydrologic variables of different GCMs are remarkably similar. The global annual anomalies of precipitation show a significant upward trend related to the upward trend of surface temperature, during the latter half of the twentieth century. While this implies an increase in the hydrologic cycle intensity, a concomitant increase of total precipitable water again leads to a decrease in the calculated global cycling rate. An analysis of the land/sea differences shows that the simulated precipitation over land has a decreasing trend while the oceanic precipitation has an upward trend consistent with previous studies and the available observations. The decreasing continental trend in precipitation is located primarily over tropical land regions, with some other

regions, such as North America experiencing an increasing trend. Precipitation trends are diagnosed further using the water tracers to delineate the precipitation that occurs because of continental evaporation, as opposed to oceanic evaporation. These diagnostics show that over global land areas, the recycling of continental moisture is decreasing in time. However, the recycling changes are not spatially uniform so that some regions, most notably over the United States, experience continental recycling of water that increases in time.

1. Introduction

The questions of how to define the water cycle intensity and whether it has changed can be addressed in several ways on both regional (Karl and Knight, 1998; Chase et al. 2003; Bosilovich and Schubert, 2001; Brubaker et al. 2001) and global scales. At the global scale, a simple method of estimating the global cycling rate or residence time uses long-term area averages of global precipitation and total water content (Chahine, 1992; Trenberth, 1998). For example, Chahine (1992) evaluated the global water cycle and storages and estimated the global atmospheric residence time (e-folding time) of water to be 10 days. While this method is computationally efficient, the assumptions, which include neglecting moisture transport in the derivation, may be restrictive. Greenhouse gas experiments that use coupled ocean-atmosphere models indicate that, as temperature increases, the precipitation rate increases in response to increasing surface evaporation, and total precipitable water (TPW) increases with the water holding capacity of the atmosphere (e.g. Roads et al. 1996; Watterson 1998; IPCC, 2001). In AGCM experiments, Yang et al (2003) show the immediate effect of CO2 warming in the atmosphere is to decrease the precipitation rate. Douville et al. (2002) found in numerical simulation that even with increased evaporation, TPW and precipitation, the global cycling rate decreased. Global warming simulations also indicate that some increased continental drying

(Wetherald and Manabe, 1999) and increased risk of flooding (Milly et al. 2002) can occur. Kumar et al. (2003) found that in AGCM simulations using the last 50 years of observed SST forcing, tropical precipitation over oceans increases with increasing SST, while tropical precipitation over land decreases with increasing SST.

Koster et al. (1986) and Joussaume et al. (1986) used passive atmospheric tracers in AGCMs to quantify the regional sources of water for global precipitation. In the present study, we have adopted this method and configured it to estimate the global cycling of water. The result is a quantitative estimate of global water cycling rate (or the inverse, called residence time) for atmospheric numerical models. This procedure for computing cycling rate does not require as many simplifications as the simple traditional method in the derivation of the water budget such as the use of long-term (monthly or annual) averages and global averages. Here, we have designed a numerical experiment to test the impact on global cycling of water of 20th century changes in SST. We also use long (50 years) simulations with observed time varying SST forcing to further study the impact of changing SSTs on the climate and cycling of water.

2. Methodology

a. Global Water Cycling

A simple calculation for determining the global water cycling rate can be derived from the atmospheric water vapor budget. If the water vapor budget is vertically integrated and area averaged, the water vapor budget reduces to,

$$\frac{\partial Q}{\partial t} = E - P . \tag{1}$$

If we, assume that no water enters the atmosphere from surface evaporation (E), the budget can be written as,

$$\frac{\partial Q}{\partial t} = -P. \tag{2}$$

Here, Q is the total precipitable water content of the atmosphere (in mm) and P is the precipitation (in mm day^{-1}). If we define a time constant, $\lambda = P/Q$ and substitute into (2), we obtain

$$\frac{\partial Q}{\partial t} = -\lambda Q. \tag{3}$$

Integrating (3) from an initial time (t_0) to a future time (t), the evolution of the total column water can be described by:

$$Q(t) = Q(t_0)e^{-\lambda t}. \tag{4}$$

Therefore, $1/\lambda$ is the e-folding time (or residence time) of water in the atmosphere. The calculation of λ typically uses long-term (monthly, yearly or climate) average total precipitable water and precipitation. The traditional approach is to use monthly global averaged precipitation and total precipitable water to determine lambda, the cycling rate of water in the atmosphere (e.g. Trenberth 1998, Douville et al 2002).

b. Model

The primary atmospheric numerical model used in this study is the Finite Volume General Circulation Model (fvGCM; Lin, 2003). The finite-volume dynamical core uses a terrain-following Lagrangian control-volume vertical coordinate system (Lin and Rood 1999; Lin 2003; Collins et al. 2003). The FVGCM dynamical core formulation includes a conservative Flux-Form Semi-Lagrangian (FFSL) transport algorithm (Lin and Rood 1996) with Gibbs oscillation-free monotonicity constraint on sub-grid distribution. The FFSL has consistent and conservative transport of air mass and absolute vorticity (Lin and Rood 1997). This feature of the system makes the FFSL particularly attractive for water vapor and passive tracer simulations.

The physical parameterizations of the fvGCM are based on NCAR Community Climate Model version 3.0 (CCM3) physics. The NCAR CCM3 parameterizations are a collection of physical processes with a long history of development and documentation (Kiehl et al. 1998). The moist physics package includes the Zhang and McFarlane (1995) deep convective scheme, which handles updrafts and downdrafts and operates in conjunction with the Hack (1994) mid- and shallow convection scheme. For radiation, the longwave radiative transfer is based on an absorptivity-emissivity formulation (Ramanathan and Downey 1986) and the shortwave radiative parameterization uses the δ-Eddington method (Briegleb 1992). The boundary-layer mixing/turbulence parameterization utilizes the "nonlocal" formulation from Holtslag and Boville (1993). In addition, the NCAR physical parameterization package includes orographic gravity wave drag based on McFarlane (1987). The land surface parameterization is that of Bonan (1998). The basic climatology of this configuration of FVGCM with CCM3 physics is described in Chang et al. (2001). Some regional aspects of the simulated hydrological cycle are discussed by Bosilovich et al. (2003), and the surface energy budget is evaluated by Betts et al. (2003).

The model also includes water vapor tracers (WVT) to quantify the geographical source of water for global precipitation (Bosilovich and Schubert, 2002; Bosilovich 2002 and Bosilovich et al. 2003). In addition to such diagnostics as the oceanic and continental sources of water, the WVTs can be used to numerically solve for (2). For example, a WVT can be defined initially equal to the model's specific humidity. This humidity is then predicted as a passive tracer (separate and distinct from the model's specific humidity prognostic variable) without a source of surface evaporation, but including tracer transport and precipitation and turbulent tendencies, using

$$\frac{\partial q_T}{\partial t} = -\nabla_3 \cdot (q_T V) + \frac{\partial q_T}{\partial t}_{turb} + \frac{\partial q_T}{\partial t}_{Prec}, \qquad (5)$$

where q_T is the three-dimensional water vapor tracer, V is the three-dimensional wind, *turb* denotes the turbulent tendency not including surface evaporation (vertically integrates to zero) and *Prec* denotes the sum of all tracer precipitation tendencies (including condensation, rain evaporation, and convective vertical movement; vertically integrates to $-P_T$). The tracer precipitation tendencies are computed proportional to the total precipitation tendency, where the proportionality is based on the ratio of tracer water to total water (Bosilovich and Schubert, 2002).

In the present experiments, we initialize a WVT equal to specific humidity at the beginning of each season (the first day of December, March, June and September) and do not permit evaporation to enter the WVT as a source. Without evaporation as a source, the water in this WVT moves around the globe while precipitating until there is little or no water left. Vertical integration and global averaging of the WVT (q_T in 5) prognostic equation results in an expression similar to (2). The difference between the two methods is that the tracer precipitation (P_T) acts to diminish tracer water at each model time step, where as the long term average of precipitation is used in the simple calculation. To determine lambda for the WVT method, we solve

$$\ln[Q_T(t)/Q_T(t_0)] = -\lambda t \tag{6}$$

assuming zero intercept (where $Q_T(t)$ is the daily global average of the vertically integrated tracer water content, and t_0 is the initial day). Figure 1 shows daily averages of the vertically integrated global average WVT content for this calculation. On day one, the WVT is nearly identical to specific humidity. The log of the daily WVT content follows a linear decrease as described by equation 6. The slope of the line estimates lambda. In this example, the linear regression of the WVT data gives lambda equal to 0.108 day^{-1} (or a residence time of 9.27 days). On the other hand, using the time average of the precipitation and total precipitable water (for the same period)

yields a residence time of 7.55 days. Using monthly mean data to calculate lambda implies that the mean precipitation rate and water content exists throughout the period, but the WVT calculation allows the precipitation rate and water content to vary in time, and any averaging is performed as a post processing step.

c. Experimental Design

The purpose of these experiments is to assess the impact of changes in the sea surface temperature (SST) and carbon dioxide concentration on the cycling of water and to study the usefulness of the WVT method for studies of the global cycling of water. The Hadley Center SST data consists of global gridded SSTs for the early 1900s through present (Rayner et al. 1996, 2003). We average the SSTs to generate mean annual cycles for the early (1902-1921) and late (1979-1998) twentieth century. We use these SSTs in 15-year climate simulations (following a 2 year spinup period). Early 1900s (1900-1920) carbon dioxide concentration from ice core measurement is 299.5 ppm (Ethridge et al. 1998). A present day value for carbon dioxide concentration is 355 ppm. We have run the following 5 AGCM experiments:

EXP1 late century SST, 355 ppm CO2

EXP2 late century SST, 299.5 ppm CO2

EXP3 early century SST, 355 ppm CO2

EXP4 early century SST, 299.5 ppm CO2

EXP5 late century SST, 710 ppm CO2

For these simulations, the spatial resolution of the fvGCM is 2°×2.5°.The simulations are designed to show the impact of SST and CO2 on the simulated atmospheric climate. We focus on the cycling of global water vapor in atmospheres/land models (described in the next section). Note that, because we are running AGCM experiment, we do not include the affects of coupled ocean

atmospheric feedbacks nor do we consider other climate forcings such as those associated with aerosols and volcanoes.

We compute the global cycling of water in two ways. The water vapor tracer method is used as described in section 2. b. At the beginning of each season (1 December, 1 March, 1 June and 1 September), the WVT is reinitialized to the value of water vapor content at that time. The WVT is predicted forward in time, using the water vapor precipitation tendencies but not surface evaporation. In this way, we can estimate the global cycling rate of water (equation 6) once a season for 15 years of each simulation by linear regression of tracer water for a 45 day period following initialization at the beginning of the season. After 45 days, the tracer water is so close to zero that the linearity does not hold well. We also compute global cycling with the traditional method using the 45-day global averages of precipitation and total water in the systems (Chahine 1992; Trenberth 1998, Douville et al. 2002).

3. Global cycling of water

a. Comparison of methods

Figure 2 shows the values of global cycling computed from the seasonal averages of total precipitable water and precipitation as well as the seasonal values computed from the WVT method for EXP1 (late twentieth century control). In the mean, the WVT method estimates a residence time that is 2.2 days longer than that based on the traditional calculation (note that each curve is associated with its own axis). The amplitude of the annual cycle of the residence time is larger for the WVT calculation, and there appears to be greater interannual variability. Figure 3a shows the EXP1 mean annual cycle and the respective annual means for both methods. The mean annual cycles of the residence time from the two global cycling methods are similar, especially in that both have a minimum in DJF. One difference is that the WVT values peak in JJA, but the traditional method produces values as large in JJA as they are in SON. The methods certainly

produce estimates that differ in interannual variability, considering that the SSTs do not have interanual variability. The range of values (maximum minus minimum) in each season is much greater for the WVT method than for the traditional calculation (Figure 3b). This result is also evident from the standard deviation of each season (Figure 3c). The WVT method calculates new water contents at the model time step, so that precipitation can only affect water vapor when there is remaining water vapor to be removed. Conversely, water vapor may remain in the simulated atmosphere longer in regions with little or no precipitation. Heavy regional precipitation, as in the tropics, may cause water to drain quickly. However, once the regional water content is small, the heavy precipitation is less a factor in the WVT cycling calculation. This is not accounted for in the traditional method using globally averaged TPW and precipitation. In this way, the water vapor tracer method produces values of residence time longer than the simple averages. While there are differences in the mean values, there are substantial similarities between the two results. Table 1 shows the correlation between the residence times computed from each method. While there is some seasonality in the correlation, namely DJF correlation is smaller than the other seasons, the two calculations are reasonably well correlated.

b. 20^{th} Century changes

In this part of the experimentation, the goal is to discern the impact of global changes that have occurred over the 20^{th} century on the cycling of water, and whether the more computationally expensive water vapor tracer calculation can provide additional information. Specifically, we examine the response of the climate system to changes in sea surface temperatures (SSTs) and carbon dioxide concentration (CO2). Figure 4 shows the mean difference in the SST between the early and late twentieth century. While there are some negative anomalies in the Pacific Ocean and at high latitude (due to sea ice variations), most of the global SST differences are positive. For example, the Indian Ocean and southern Atlantic Ocean are

nearly 0.5K warmer on average. The global mean is 0.37 K warmer in the late century compared to the early century (Figure 5). While SSTs are warmer during all seasons in the late century, there is a seasonal cycle with JJA having the largest seasonal increase.

Figure 6 shows the mean differences in precipitation and TPW between EXP1 and all the other experiments. The combined effect of early and late century SST and CO2 are shown in the differences between EXP1 and EXP4. The precipitation anomalies vary between regions, and most of the significant impact is over the ocean. The tropical precipitation patterns show positive and negative anomalies because of the shifting circulations, rather than a correlation to local SST differences (Figure 4). However, the model indicates that precipitation over the Amazon decreases for the late 20th century, while the precipitation over the southwestern United States increases. This result is qualitatively similar to that found by Kumar et al (2003) for the tropical precipitation over land. On the other hand, TPW increases almost everywhere, except where the SST differences are weak or negative (e.g. the central North Pacific and tropics west of South America). The difference of EXP1 and EXP2 shows the direct impact of the change of CO2 over the 20th Century, which is much less than the impact of the changes in SST alone (Figure 6 b,c,f,g). Doubling the CO2 (EXP5) increases the TPW and decreases the precipitation, compared to EXP1. However, the precipitation decrease is over ocean, where there is no feedback (i.e. surface temperature changes). The precipitation increases are over land, where there is feedback with the land surface parameterization, for example in Africa and the Amazon. The net result is that the global precipitation decreases with increasing CO2. A similar result was found by Yang et al (2003), where the increased CO2 (with prescrbed SST) decreased the radiative cooling, which was offset by a decrease in latent heating due to precipitation.

In a regional analysis, Chase et al. (2003) evaluated observations and the NCEP reanalysis to determine trends in large monsoon regions (Southeast Asia, East and West Africa and

Australia). All the cases studied showed decreasing trends in precipitation, however, the precipitation trends were not found to be significantly different from zero in Southeast Asia and Western Africa. In the present simulation, there are few significant differences in the monsoon regions (Figure 6a). However, Eastern Africa does have an increase of precipitation from the early to late 20th century. In addition, the Mexican monsoon region experiences a local increase in precipitation.

Figure 7 shows the time and global average residence times computed from the WVT method and the simple method for each experiment. A mean difference of nearly 2.2 days is found between the methods for each experiment. In comparing the early 20th century experiment (EXP4) and the late century experiment (EXP1), the residence time of water in the atmosphere increases by approximately 0.2 days. Increasing the CO2 and increasing the SST both act to increase the residence time, though the impact of 20th century CO2 is less than that of the SST. A doubling of the CO2, while keeping the SST at the late 20th century values, shows a 0.25 day increase in the residence time compared to the present day control. These simulations show that an increase in SST or CO2 can increase the TPW lessxn impact on precipitation (Table 2), thereby increasing the residence time of water in the atmosphere and slowing of the global water cycling rate. The similarity between the two cycling rate methods suggests that the basic response of the system to climate forcing can be reasonably investigated using the simple method. Of course, if the absolute magnitude or the interannual variability of residence time are required, the simple method data may be insufficient. In the next section, we evaluate the water cycling results further with real time varying SSTs in several different global models.

4. 50-year model integrations

a. FVGCM

To further investigate the cycling rate changes related to SST increases, a 50 year model integration was performed with the FVGCM at 2°×2.5° horizontal resolution. Hadley Centre monthly varying SSTs provide the boundary forcing for the GCM for the period 1949 – 1998, but the trend of CO2 was not included (a present day value was used). Figure 8 shows the time series of annual and global averaged surface temperature, precipitation, TPW and residence time. The time series of temperature show slight cooling from the 1950's through mid-1970s, and increasing temperatures from the 1970's through 1990's. Precipitation and TPW appear to correlate well with the surface temperature. The residence time (TPW/P) shows a mostly increasing trend (in contrast to the surface temperature time series) across the period. Surface evaporation is not shown, but its evolution is nearly identical to that of the precipitation (annually and globally averaged). Overall, the annual global means of precipitation, surface temperature, TPW and residence time are all positively correlated (Table 3). In the next section, we will compare the apparent fvGCM trend in the hydrologic cycle with those of other models.

b. Ensemble Simulations

In participating in the Climate of the Twentieth Century Project (Folland et al. 2002), several GCM research groups are integrating their models for long periods of the twentieth century. In particular, ensemble simulations from NASA's Seasonal to Interannual Prediction Project (NSIPP, 9 members) and the Center for Ocean, Land and Atmosphere (COLA, 10 members) are available for analysis. Here, we compare the ensemble means of these GCM integrations with the single FVGCM simulation discussed in the previous section. The COLA AGCM uses the dynamical core described by Kiehl et al. (1998) with semi-Lagrangian advection of moisture (Kinter et al. 1997; Dirmeyer and Zeng, 1999; Schneider 2002). The land

parameterization is the Simplified Biosphere model (SSiB, Xue et al. 1991; Xue et al. 1996). The NSIPP (version 1) AGCM uses the dynamical core described by Suarez and Takacs (1995). The land parameterization is the Mosaic land surface model (Koster and Suarez, 1992). Both COLA and NSIPP AGCMs use the relaxed Arakawa-Schubert parameterization for deep convection (Moorthi and Suarez, 1992). The NSIPP-1 model has been used in several predictability studies (Pegion et al. 2000; Schubert et al. 2002 and Schubert et al. 2003). Straus et al. (2003) recently intercompared the NSIPP and COLA AGCMs in seasonal prediction experiments. The COLA model simulations are for the period 1949 – 1997. All the other data sets are compared through 1998. The NSIPP and COLA simulations examined here are the initial contributions to the C20C project; in these experiments only the SST forcing is included (CO2 is fixed at the present day concentration).

Each of the models has different mean states of the water cycle, so we focus on the anomalies from the 50-year means. Figure 9 shows the globally averaged annual anomalies of surface temperature, precipitation, TPW and residence time (TPW/P). In general, the GCMs anomalies are all very well correlated, with increasing trends in precipitation, TPW and residence time. The values of the trends are presented in Table 4. The significance of the trends is tested by computing the t-statistic for the trend line, and each trend is found to be significant at the 99% level (except where noted in the table). At issue is then how the water cycle intensity is defined. In all the models, both precipitation and evaporation (not shown) are increasing, which may be interpreted as an intensification of the water cycle. On the other hand, the residence time is increasing, so that TPW must be increasing faster than the precipitation. Therefore, the cycling rate of water (inverse of residence time) is decreasing which may be interpreted as a lessening of the intensity of the water cycle. This result is similar to that found by Douville et al. (2002) using

a coupled atmosphere ocean GCM, and that of Roads et al (1998) using the Community Climate Model version 3.

c. Differences between Continental and Oceanic Precipitation

While the SSTs are driving the atmospheric changes, the role of the land surface is not clear. For example, the differences in Figure 6h seem to be mostly related to the land-atmosphere feedback. Figure 10a shows the temporal correlation of the detrended annual time series residence time with the FVGCM annual surface temperature fields. An ENSO-like pattern is apparent in the Pacific Ocean extending into the Indian Ocean. However, the largest correlations are over the Caribbean Sea, and extend across the tropical Atlantic Ocean. The maximum correlations also extend across the Amazon River Basin. In addition, a substantial area of the Asian continent is positively correlated to the residence time. It seems reasonable that the residence time may be related to the evaporation through surface temperature. However, the correlation of global residence time with surface evaporation shows little resemblance to the correlation with surface temperature (Figure 10b). For example, there is a negative correlation between the residence time and Amazonian evaporation. The correlation of residence time with TPW more closely reflects the patterns of correlation with surface temperature (Figure 10c), which may indicate that the relationship of residence time with SST may be more associated with the water holding capacity of the atmosphere than the surface evaporation. We made similar comparisons with the NSIPP and COLA ensemble mean data, and the patterns are similar, but the correlations are stronger as would be expected for ensemble means (figures not shown).

We also averaged the precipitation over land and oceanic areas separately (Figure 11). Contrary to the global average of precipitation, the land average of precipitation decreases across the 50 year period. This agrees with the Global Historical Climatology Network (GHCN) land gage observations (Vose et al. 1992), despite the irregularity of the observing network. Oceanic

average of precipitation increases in time. The magnitudes of the trends for land and oceanic averages are more than the global average (Table 5). The trends are quite similar for each model and the GHCN observations. In Figure 12, the precipitation trend is computed at each grid point for the FVGCM, NSIPP and COLA GCMs. There are remarkable regional similarities in the precipitation trends. Notable positive trends over the tropical Pacific Ocean, Indian Ocean and Kurashio Current are apparent in each model. Notable negative trends over the Gulf of Mexico, Caribbean Sea, Amazon, central Africa and north central Pacific Ocean are likewise apparent in each model. The global decreases in continental precipitation are mostly related to the regional decreases in the tropical land areas (central Africa and Amazon). This agrees with the analysis of tropical precipitation in AGCM simulations by Kumar et al. (2003). The average decrease in precipitation over land is not uniform, as precipitation over the contiguous United States is generally increasing in all the GCMs. Figure 12d shows the trends of GHCN gage precipitation gridded at 5 degrees resolution. The large-scale trends in the central United States and Africa noted in the model simulation agree well with the observations.

In this FVGCM experiment, the water vapor tracers (WVTs) were configured to represent geographical sources of water, as in Bosilovich and Schubert (2002) and Bosilovich et al. (2003). Specifically, WVTs were implemented to tag the surface evaporation from the continental and oceanic source regions. Figure 13a shows the time series of globally averaged FVGCM continental evaporation. The land evaporation is generally decreasing (see also Table 6). The precipitation over land from both land sources and oceanic sources are decreasing (Table 6 and Figure 13 b and c). Oceanic sources of precipitation over land appear to stabilize for the last 25 years of the simulation (when surface temperatures are generally increasing). Continental sources of precipitation over land decrease over the 50-year period. However, the decrease of land evaporation does not extend to the most recent 25 years.

Figure 14 a and b shows the trend of precipitation from land sources and the trend of precipitation from oceanic sources. While these trends generally follow that of the total precipitation (Figure 12a), several distinct differences are apparent. First, while trends in precipitation from oceanic sources are positive over the central United States, the values are relatively small and not statistically significant. However, the trend of precipitation from continental sources over the central United States is more significant. This differs from the tropical land regions (specifically the Amazon and central Africa) where both trends in land and oceanic sources are large and comparable. The map of evaporation trend (Figure 14c) is remarkably similar to the map of total precipitation trend (Figure 12a, the spatial correlation of the significant values in these two figures is 0.62).

Table 7 shows the trend of area averaged precipitation, evaporation and surface temperature for the Mississippi and Amazon River basins. The increasing trend of precipitation in the Mississippi basin is related to the increasing trend of precipitation from continental sources. This result agrees with Brubaker et al (2001) who found that continental recycling of water, determined from observations and reanalysis data, is increasing in the Mississippi River basin. The evaporation within the Mississippi River basin is likewise increasing, but surface temperature changes do not experience a significant trend. In the Amazon, the precipitation trend is the result of changes in both continental and oceanic sources of water. The Amazon evaporation experiences little change over the whole period, but a more decreasing trend in the last half of the 50-year period, while surface temperatures continually increase. While it is not the purpose of this paper to discuss the changes of regional water cycles in-depth, this analysis demonstrates the range of regional variability of the water cycle intensity changes. Furthermore, the changes in continental precipitation and local cycling of water are likely seasonally dependent (as discussed by Wetherald and Manabe, 1999).

5. Summary and conclusions

In this study, we estimate the global cycling rate of water in global atmospheric models using two methods. The traditional method can be applied to any model simulation, but uses simplifying assumptions that may affect the result. The water vapor tracer (WVT) method for global cycling rate utilizes the capability of models passive constituent tracers to predict a separate water vapor variable (parallel to specific humidity) that solves the water vapor budget without a source of surface water (evaporation). In contrast, the traditional cycling rate calculations simply use time averaged precipitation and total precipitable water diagnostics, and is more easily applied to models simulations and existing observations. While the WVT method did show greater interannual variability and a higher mean values than the simpler method, the mean sensitivity of both methods to climate perturbations was comparable.

Climate simulations using mean sea surface temperature and CO2 forcings representative of the early and late twentieth century were performed with the fvGCM. These showed that the global precipitation changed little with 20th century climate SST changes. However, the TPW increased with the increasing temperatures and so did the residence time of water vapor in the atmosphere. These simulations suggested that the global water cycling rate slowed for the simulation of 20th century climate. The processes that lead to this conclusion have also been found in other GCM simulations (Roads et al. 1998; Douville et al. 2002). However, in these studies, the evolution of the water cycle or the significance of the changes were not explored.

The evolution of the hydrologic cycle was tested using several 50-year model simulations forced with observed time varying SSTs. The SST warming in the 50-year simulations drives increased evaporation and precipitation. Taken in isolation, this implies the water cycle is intensifying. On the other hand, the total precipitable water increases with warming and therefore the residence time of water increases, despite the increase of precipitation. The fact that water is

spending more time in the atmosphere implies that the global cycling rate is decreasing. The 50-year simulations from three models with different physical parameterizations all provide the same conclusions. The increasing trends of precipitation (and evaporation), TPW and residence time were statistically significant in all the GCMs evaluated.

Some regional correlations between the global residence time and SST were identified, including strong correlations to the tropical Pacific SST and to the Caribbean Sea. While the Amazon surface temperatures correlate to the global cycling rate, the corresponding surface evaporation did not. In the global average sense, the precipitation trend over land is decreasing (similar result as Kumar et al. 2003 for the tropics), while the trend over oceans increases. The magnitude of these trends exceeds that of the total global average (land and ocean combined) so that the increasing global trend is not necessarily representative of the globe. Furthermore, the contrasting land and ocean trends are not universally applicable to all regions. For example, the precipitation over the North American continent is increasing, while the precipitation trend over the Gulf of Mexico is decreasing.

Tracer diagnostics that delineate ocean and continental sources of water show that the continental sources of water for precipitation over land decrease continually through out the last 50 years of the 20th century. The ocean sources of precipitation over land have virtually no trend over land in the last 25 years of the 20th century. There are distinct and significant changes in different directions depending on the region. Continental cycling of water appears to be decreasing in time, except for the central United States, where continental cycling may be increasing. Further study is needed with a regional focus and with more detailed diagnostics that can quantify the local recycling rates.

Acknowledgments

We would like to thank Dr. S.-J. Lin, Dr. Jiun-Dar Chern and Jon Radakovich for their support of the fvGCM in these studies. Michael Kistler and Philip Pegion provided support for the NSIPP C20C simulation, James Kinter provided the COLA C20C GCM data online. Discussions with Drs. Alan Betts, Paul Dirmeyer, Robert Atlas, Yogesh Sud and John Roads were particularly useful in evaluating these results. This work was supported by the NOAA/NASA GAPP PACS Warm Season Precipitation Initiative and also by the NASA Global Water and Energy Cycle (GWEC) Program.

6. References

Betts, A. K., J. H. Ball, M. G. Bosilovich, P. Viterbo, Y Zhang and W. B. Rossow, 2003: Intercomparison of Water and Energy Budgets for Five Mississippi Sub-basins between ECMWF Reanalysis (ERA-40) and NASA-DAO fvGCM for 1990-1999. *J. Geophys. Res.*, **108(D16)**, 8618, doi:10.1029/2002JD003127.

Bonan, G. B., 1998: The land surface climatology of the NCAR land surface model coupled to the NCAR Community Climate Model, *J. Clim.*, **11**, 1307 – 1326.

Bosilovich, M. G., 2002: On the Vertical Distribution of Local and Remote Sources of Water for Precipitation, *Meteorol. Atmos. Phys.*, **80**, 31-41.

Bosilovich, M. G., and S. D. Schubert, 2001: Precipitation recycling in the GEOS-1 data assimilation system over the central United States, *J. Hydromet.*, **2**, 26 – 35.

Bosilovich, M. G. and S. D. Schubert, 2002: Water vapor tracers as diagnostics of the regional hydrologic cycle, *J. Hydromet.*, **3**, 149-165.

Bosilovich, M. G., Y. C. Sud, S. D. Schubert and G. K. Walker, 2003: Numerical simulation of the North American monsoon water sources. *J. Geophys. Res.,* 108(D16), 8614, doi:10.1029/2002JD003095.

Briegleb, B. P., 1992: Delta-Eddington approximation for solar radiation in the NCAR Community Climate Model. *J. Geophys. Res.*, **97**, 7603-7612.

Brubaker, K. L., P. A. Dirmeyer, A. Sudradjat, B. S. Levy and F. Bernal, 2001: A 36-year climatological description of the evaporative sources of warm-season precipitation in the Mississippi River Basin. *J. Hydromet.*, **2**, 537-557.

Chahine, M. T., 1992: The hydrological cycle and its influence on climate, *Nature*, **356**, 373-380.

Chang, Y., S. D. Schubert, S.-J. Lin, S. Nebuda and D.-W. Shen, 2001: The climate of the FVCCM-3 Model, NASA/TM-2001-104606, vol. 20, pp. 127.

Chase, T. N., J. A. Knaff, R. A. Pielke, E. Kalnay, 2003: Changes in global monsoon circulations since 1950. *Natural Hazards*, **29**, 229–254.

Collins, W. D., J. J. Hack, B. A. Boville, P. J. Rasch, D. L. Williamson, J. T. Kiehl, B. Brieglib, C. Bitz, S.-J. Lin, and R. B. Rood, 2003: Description of the NCAR Community Atmosphere Model (CAM2), *NCAR/TN In Preparation.*

Dirmeyer, P. A., and F. J. Zeng, 1999: An update to the distribution and treatment of vegetation and soil properties in SSiB. COLA Technical Report 78 [Available from the Center for Ocean-Land-Atmosphere Studies, 4041 Powder Mill Road, Suite 302, Calverton, MD 20705 USA], 25 pp.

Douville, H., F. Chauvin, S. Planton, J.-F. Royer, D. Salas-Melia and S. Tyteca, 2002: Sensitivity of the hydrological cycle to increasing amounts of greenhouse gasses and aerolsols. *Clim. Dyn.*, **20**, 45-68.

Etheridge D.M., L.P. Steele, R.L. Langenfelds, R.J. Francey, J.-M. Barnola and V.I. Morgan, 1998: Historical CO2 records from the Law Dome DE08, DE08-2, and DSS ice cores. In Trends: A Compendium of Data on Global Change. Carbon Dioxide Information Analysis Center, Oak Ridge National Laboratory, U.S. Department of Energy, Oak Ridge, Tenn., U.S.A

Folland, C., J. Shukla, J. Kinter, and M. Rodwell, 2002: The Climate of the Twentieth Century Project. CLIVAR Exchanges News Letter, v. **7**, no. 2, 37-39.

Hack, J. J., 1994: Parameterization of moist convection in the National Center for Atmospheric Research Community Climate Model (CCM2). *J. Geophys. Res.*, **99**, 5551-5568.

Holtslag, A. A. M., and B. A. Boville, 1993: Local versus nonlocal boundary-layer diffusion in a global climate model. *J. Climate*, **6**, 1825-1842.

IPCC, 2001: Intergovernmental Panel on Climate Change, Climate Change 2001 - The Scientific Basis. Houghton, JT (ed.), Cambridge University Press, Cambridge, UK, 881 pp.

Joussaume, S., R. Sadourny and C. Vignal, 1986: Origin of precipitating water in a numerical simulation of July climate, *Ocean-Air Interactions*, **1**, 43 – 56.

Karl, T.R. and R.W. Knight, 1998: Secular trends of precipitation amount, frequency and intensity in the United States. *Bull. Am. Met. Soc.*, **79**, 231–241.

Kiehl, J. T., J. J. Hack, G. B. Bonan, B. A. Boville, D. L. Williamson, and P. J. Rasch, 1998: The National Center for Atmospheric Research Community Climate Model (CCM3), *J. Clim.,* **11**, 1131-1149.

Kinter, J. L., D. DeWitt, P. A. Dirmeyer, M. J. Fennessy, B. P. Kirtman, L. Marx, E. K. Schneider, J. Shukla, and D. M. Straus, 1997: The COLA atmosphere-biosphere general circulation model. Volume 1: Formulation. COLA Technical Report 51 [Available from the Center for Ocean-Land-Atmosphere Studies, 4041 Powder Mill Road, Suite 302, Calverton, MD 20705 USA], 46 pp.

Koster, R. D. and M. J. Suarez, 1992: A comparative analysis of two land surface heterogeneity representations, *J. Climate*, **5**, 1379-1390.

Koster, R. D., J. Jouzel, R. Suozzo, G. Russell, W. Broecker, D. Rind, and P. Eagleson, 1986: Global sources of local precipitation as determined by the NASA/GISS GCM, *Geophys. Res. Let.*, **13**, 121-124.

Kumar, A., F. Yang, L. Goddard and S. D. Schubert, 2003: Differing trends in the tropical surface temperatures and precipitation over land and oceans. Accepted for publication in the Journal of Climate.

Lin, S.-J., 2003: A "vertically Lagrangian" finite-volume dynamical core for global models. *Submitted to Mon. Wea. Rev.*

Lin, S.-J., and R. B. Rood, 1996: Multidimensional flux form semi-lagrangian transport schemes, *Mon. Wea. Rev.*, **124**, 2046 – 2070.

Lin, S.-J., and R. B. Rood, 1997: An explicit flux-form semi-Lagrangian shallow-water model on the sphere, *Q. J. Roy. Meteor. Soc.*, **123**, 2477 – 2498.

Lin, S.-J., and R. B. Rood, 1999: Development of the joint NASA/NCAR general circulation model. 13th Conf. on Numerical Weather Prediction, September 12-17, Denver, CO.

McFarlane, N. A., 1987: The effect of orographically excited wave drag on the general circulation of the lower stratosphere and troposphere. *J. Atmos. Sci.*, **44**, 1775-1800.

Milly, P.C.D, R. T. Wetherald, K. A. Dunne and T. L. Delworth, 2002: Increasing risk of great floods in a changing climate. *Nature*, **415**, 514-517.

Moorthi, S. and M. J. Suarez, 1992: A parameterization of moist convection for general circulation models. *Mon. Wea. Rev.*, **210**, 978-1002.

Pegion, P. J., S. D. Schubert and M. J. Suarez, 2000: An assessment of the predictability of northern winter seasonal means with the NSIPP 1 AGCM, NASA Tech. Memo. 104606, vol. 18, Goddard Space Flight Center, Greenbelt MD 20771.

Ramanathan, V., and P. Downey, 1986: A nonisothermal emissivity and absorptivity formulation for water vapor. *J. Geophys. Res.*, **91**, 8649-8666.

Rayner, N.A., Horton, E.B., Parker, D.E., Folland, C.K., and Hackett, R.B., 1996: Version 2.2 of the global sea-ice and sea surface temperature data set, 1903-1994. Climate Research Technical Note No. 74, The Met Office.

Rayner, N. A., D. E. Parker, E. B. Horton, C. K. Folland, L. V. Alexander, D. P. Rowell, E. C. Kent, and A. Kaplan, 2003: Global analyses of sea surface temperature, sea ice, and night marine air temperature since the late nineteenth century, *J. Geophys. Res.*, **108(D14)**, 4407, doi:10.1029/2002JD002670.

Roads, J.O., S. Marshall, R. Oglesby and S.-C. Chen, 1996: Sensitivity of the CCM1 hydrological cycle to CO2. *J. Geophys. Res.*, **101**, 7321-7339.

Roads, J. O., S. C. Chen, S. Marshall and R. Oglesby, 1998: Atmospheric moisture cycling rates. *GEWEX News*, **8**, 7-10.

Schubert, S. D., M. J. Suarez, P. J. Pegion, M. A. Kistler and A. Kumar, 2002: Predictability of zonal means during boreal summer. *J. Clim.*, **15**, 420-434.

Schubert, S. D., M. J. Suarez, P. J. Pegion, R. D. Koster and J. T. Bacmeister, 2003: Causes of long-term drought in the United States great plains. *J. Climate*, Submitted.

Schneider, E. K., 2002: The causes of differences between equatorial Pacific SST simulations of two coupled ocean-atmosphere general circulation models. J. Climate, 15, 449-469.

Straus, D., D. Paolino, J. Shukla, S. D. Schubert, M. J. Suarez, A. Kumar, and P. Pegion, 2003: Predictability of the seasonal mean atmospheric circulation during autumn, winter and spring. *J. Clim.*, Accepted for publication.

Suarez, M. J. and L. L. Takacs, 1995: Documentation of the Aries-GEOS dynamical core: Version 2, NASA Tech Memo 104606, vol. 5, pp. 45.

Trenberth, K. E., 1998: Atmospheric moisture residence times and cycling: Implications for rainfall rates and climate change. *Climatic Change*, **39**, 667-694.

Watterson, I. G., 1998: An analysis of the global water cycle of present and doubled CO2 climates simulated by the CSIRO general circulation model. *J. Geophys. Res.*, **D18**, 23113-23129.

Wetherald, R. T. and S. Manabe, 1999: Detectability of summer dryness caused by greenhouse warming. *Climatic Change*, **43**, 495-511.

Vose, R., R. Schmoyer, P. Steurer, T. Peterson, R. Heim, T. Karl and J. Eischeid, 1992: The Global Historical Climatology Network: Long-term Monthly Temperature, Precipitation Sea Level Pressure and Station Pressure data. ORNL/CDIAC-53,NDP-041. Carbon Dioxide Information Analysis Center, Oak Ridge National Laboratory, Oak Ridge Tennessee.

Xue, Y., P. J. Sellers, J. L. Kinter and J. Shukla, 1991: A simplified Biosphere model for global climate studies. *J. Climate*, **4**, 345-364.

Xue, Y., F. J. Zeng, and C. A. Schlosser, 1996: SSiB and its sensitivity to soil properties - a case study using HAPEX-Mobilhy data. *Global and Planetary Change*, **13**, 183-194.

Yang, F., A. Kumar, M. E. Schlesinger and W. Wang, 2003: Intensity of hydrological cycles in warmer climates. *J. Clim.*, **16**, 2419-2423.

Zhang, G. J., and N. A. McFarlane, 1995: Sensitivity of climate simulation to the parameterization of cumulus convection in the Canadian Climate Centre general circulation model. *Atmos.-Ocean*, **33**, 407-446.

7. Tables

Table 1 Correlation between WVT and simple method residence times for the 15 years of the EXP1. "Annual Cycle" is a correlation for all seasons in all years, and "Annual Means" is the correlation of the annual means of all 15 years.

Period	Correlation
DJF	0.44
MAM	0.74
JJA	0.84
SON	0.73
Annual Cycle	0.89
Annual Means	0.64

Table 2 15-year means of global precipitation (P) and total precipitable water (TPW) in each climate experiment.

15-year Avg	P (mm day^{-1})	TPW (mm)
EXP1	3.05	24.84
EXP2	3.07	24.78
EXP3	3.00	23.94
EXP4	3.02	23.93
EXP5	3.00	25.09

Table 3 Correlation between globally and annually averaged time series of precipitation (P), total precipitable water (TPW), global residence time (TPW/P) and surface temperature (T_s). Correlations using detrended time series are in parentheses.

FVGCM	*P*	*TPW*	T_s
TPW	0.89(0.83)		
T_s	0.84(0.75)	0.95(0.90)	
TPW/P	0.66(0.47)	0.93(0.88)	0.89(0.81)

Table 4 Trends of surface temperature, precipitation, total precipitable water (TPW), and residence time (TPW/P) for the periods (a) 1949 – 1998 and (b) 1974 – 1998. The units of the variables are the amount of change per 50 years. Using t-statistic, all trends are significant (the trend is significantly different from 0) at the 1% level (p-value <0.01), except the italicized values, which are significant at 5%. COLA data are evaluated through 1997.

(a) 1949-1998

Trends (per 50yr)	Ts (K)	P (mm d^{-1})	TPW (mm)	TPW/P (days)
FVGCM	0.32	0.04	0.71	0.13
NSIPP	0.30	0.03	0.60	0.12
COLA	0.34	*0.02*	0.64	0.14

(b) 1974-1998

Trends (per 50yr)	Ts (K)	P (mm d^{-1})	TPW (mm)	TPW/P (days)
FVGCM	0.90	0.13	1.78	0.26
NSIPP	0.85	0.10	1.83	0.34
COLA	0.93	0.11	1.85	0.31

Table 5 Trends as in Table 4a except for precipitation averages over land and oceanic regions only. Antarctica is considered in the oceanic average.

Trend (per 50 yr)	P Land (mm d^{-1})	P Ocean (mm d^{-1})
FVGCM	-0.12	0.10
NSIPP	-0.08	0.17
COLA	-0.14	0.08
GHCN	*-0.06*	

Table 6 Trends as in Table 4, except for the land average time series of evaporation, precipitation that originated as land evaporation and precipitation that originated as oceanic evaporation. The trends are computed for the 50 year period and the last 25 year period.

Using t-statistic, all trend are significant (the trend is significantly different from 0) at the 1% level (p-value <0.01), except the italicized values, which are significant at 5%. Grey shaded cells are not significant at 5%. The units are trend of precipitation in mm day^{-1} per 50 years.

Trend (per 50 year)	FVGCM Land Average 50 yrs. (mm day^{-1})	FVGCM Land Average 25 yrs. (mm day^{-1})
Evaporation	*-0.016*	**0.006**
P(Land E)	-0.060	-0.062
P(Ocean E)	-0.062	**-0.020**

Table 7 Regional trends in the Mississippi River Basin (MRB) and Amazon River Basin (AMZ) of total precipitation (P), precipitation from land evaporation (P_l), precipitation from oceanic evaporation (P_o), Evaporation within the region (E) and surface temperature (T_s). The units are mm day^{-1} and K, per 50 years. Values are significant at 5%, except italicized (10%) and gray shaded (not significant at 10%).

MRB	Trend (1949-1998)	Trend (1974-1998)
P	*0.16*	**0.30**
P_l	0.16	*0.23*
P_o	**0.00**	**0.07**
E	0.10	*0.18*
T_s	**0.10**	**0.77**
Amazon		
P	-0.40	-0.84
P_l	-0.26	-0.43
P_o	*-0.14*	*-0.41*
E	**0.01**	*-0.15*
T_s	0.47	1.25

8. List of Figures

Figure 1. Time series of a water vapor tracer (Log of the tracer divided by its day one average value) initialized equal to the prognostic specific humidity. Precipitation and transport are permitted and evaporation is not included in the tracer budget. The solid line indicates the linear regression of the data assuming zero intercept. The slope is the global cycling rate and its inverse is the residence time of water in the atmosphere.

Figure 2 Time series of seasonal residence time ($1/\lambda$) as diagnosed from the WVT method (scale on left axis) and the simple seasonal global average TPW and precipitation (scale on right axis) for 15 years of EXP1 (using late 20^{th} century SST and CO2).

Figure 3 EXP1 seasonal and annual averages of residence time (a), difference of the seasonal maximum and minimum residence time (b), and the standard deviation of the seasonal residence time (c) for the WVT method (white) and simple method (black).

Figure 4 Annual mean SST difference for the late century minus early century (contours at -0.5 -0.2 -0.1 0 0.1 0.2 0.5 1.0 1.5 2.0 Kelvin). Color shaded temperature differences are significant at the 5% level based on a t-test.

Figure 5 Global average seasonal and annual difference of late century minus early century SST (Kelvin).

Figure 6 Mean difference of EXP1 precipitation and TPW with each of the other experiments. Only values significant at the 5% level of the t-test between each experiment are plotted.

Figure 7 15-year average global mean residence time computed from WVTs (black bar, left axis) and the simple mean Q/P calculation (white bar, right axis).

Figure 8 FVGCM global and annual averaged (a) surface temperature, (b) precipitation, (c) total precipitable water, and (d) residence time (computed from the annual means of precipitations and TPW).

Figure 9 Global and annual average anomalies from long term means for (a) surface temperature, (b) precipitation, (c) total precipitable water, and (d) residence time. NSIPP and COLA GCM data are ensemble averages of 9 and 10 members, respectively.

Figure 10 Map of the temporal correlation between the FVGCM detrended time series of annual residence time (as in Figure 9) and annual FVGCM (a) surface temperature (b) evaporation and (c) total precipitable water.

Figure 11 Annual average anomalies from long-term means for (a) precipitation at global land grid points and (b) precipitation at global ocean gridpoints (including the Antarctic continent). The green dots are the global land averaged GHCN gage precipitation data.

Figure 12 Map of precipitation trends at model gridpoints for (a) FVGCM, (b) NSIPP (c) COLA GCMs and (d) GHCN gage data. The units are mm day^{-1} per 50 years. For the GCMs, trends significant at 5% from t-tests are color shaded, and all values are contoured in black. The 5% significant trends in the GHCN observations are denoted by crosshatched boxes.

Figure 13 Annual averages of land grid point (a) evaporation, (b) precipitation that occurs from land evaporation and (c) precipitation that occurs from oceanic evaporation (not including the Antarctica continent in the spatial average).

Figure 14 Map of trends at model gridpoints for the FVGCM (a) precipitation that has a continental evaporative source, (b) precipitation that has an oceanic evaporative source and (c) surface evaporation. The regions in (a) outlined in green denote the areas for Mississippi River and Amazon River basin averages.

9. Table Captions

Table 1 Correlation between WVT and simple method residence times for the 15 years of the EXP1. "Annual Cycle" is a correlation for all seasons in all years, and "Annual Means" is the correlation of the annual means of all 15 years.

Table 2 15-year means of global precipitation (P) and total precipitable water (TPW) in each climate experiment.

Table 3 Correlation between globally and annually averaged time series of precipitation (P), total precipitable water (TPW), global residence time (TPW/P) and surface temperature (T_s).

Table 4 Trends of surface temperature, precipitation, total precipitable water (TPW), and residence time (TPW/P) for the periods (a) 1949 – 1998 and (b) 1974 – 1998. The units of the variables are the amount of change per 50 years. Using t-statistic, all trends are significant (the trend is significantly different from 0) at the 1% level (p-value <0.01), except the italicized values, which are significant at 5%. COLA data are evaluated through 1997.

Table 5 Trends as in Table 4a except for precipitation averages over land and oceanic regions only. Antarctica is considered in the oceanic average.

Table 6 Trends as in Table 4, except for the land average time series of evaporation, precipitation that originated as land evaporation and precipitation that originated as oceanic evaporation. The trends are computed for the 50 year period and the last 25 year period. Using t-statistic, all trend are significant (the trend is significantly different from 0) at the 1% level (p-value <0.01), except the italicized values, which are significant at 5%. Grey shaded cells are not significant at 5%.

Table 7 Regional trends in the Mississippi River Basin (MRB) and Amazon River Basin (AMZ) of total precipitation (P), precipitation from land evaporation (P_l), precipitation from oceanic evaporation (P_o), Evaporation within the region (E) and surface temperature (T_s). The units are mm day^{-1} and K, per 50 years. Values are significant at 5%, except italicized (10%) and gray shaded (not significant at 10%).

10. Figures

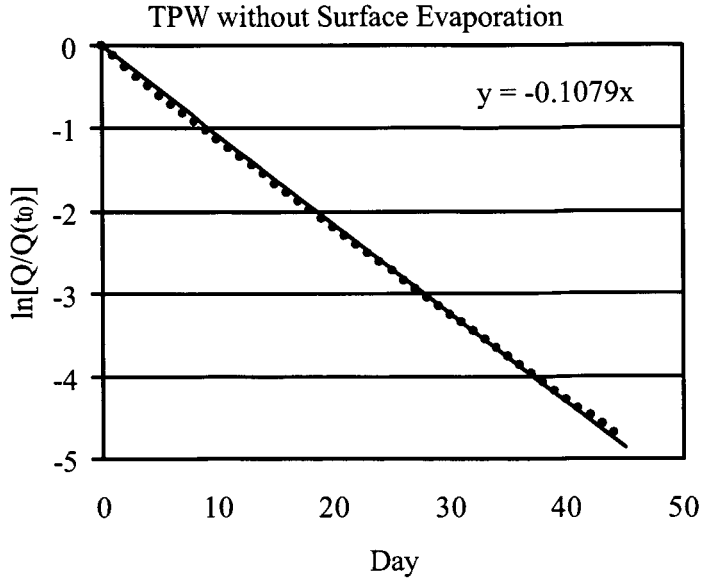

Figure 1. Time series of a water vapor tracer (Log of the tracer divided by its day one average value) initialized equal to the prognostic specific humidity. Precipitation and transport are permitted and evaporation is not included in the tracer budget. The solid line indicates the linear regression of the data assuming zero intercept. The slope is the global cycling rate and its inverse is the residence time of water in the atmosphere.

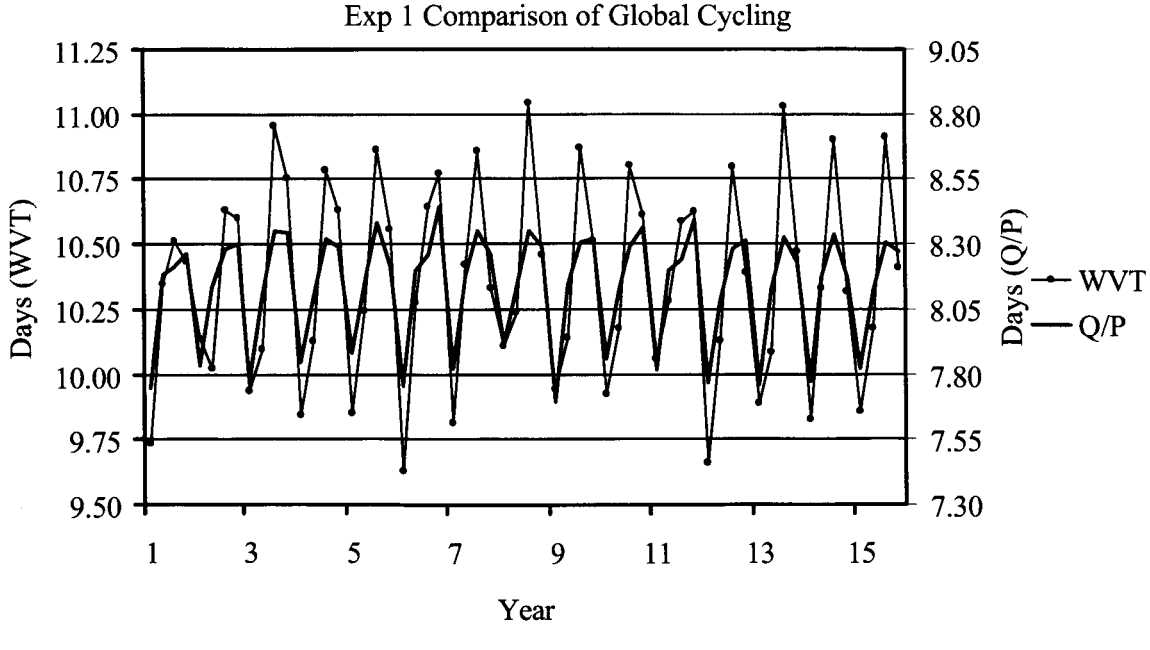

Figure 2 Time series of seasonal residence time ($1/\lambda$) as diagnosed from the WVT method (scale on left axis) and the simple seasonal global average TPW and precipitation (scale on right axis) for 15 years of EXP1 (using late 20th century SST and CO2).

10. Figures

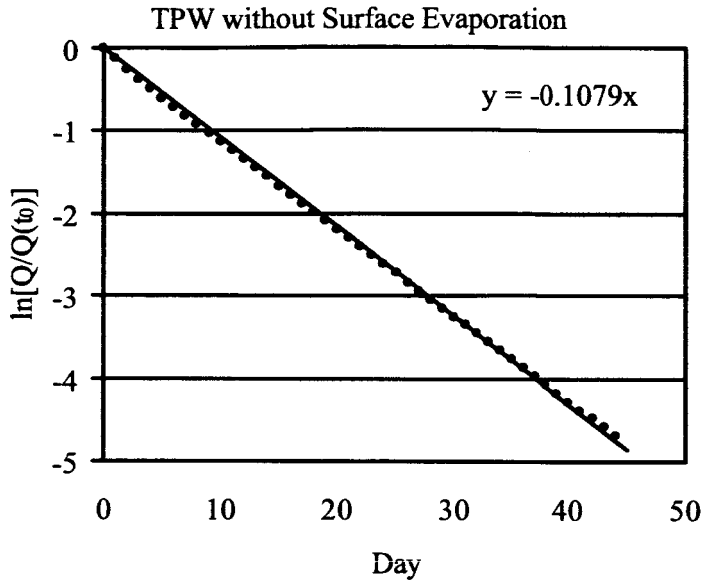

Figure 1. Time series of a water vapor tracer (Log of the tracer divided by its day one average value) initialized equal to the prognostic specific humidity. Precipitation and transport are permitted and evaporation is not included in the tracer budget. The solid line indicates the linear regression of the data assuming zero intercept. The slope is the global cycling rate and its inverse is the residence time of water in the atmosphere.

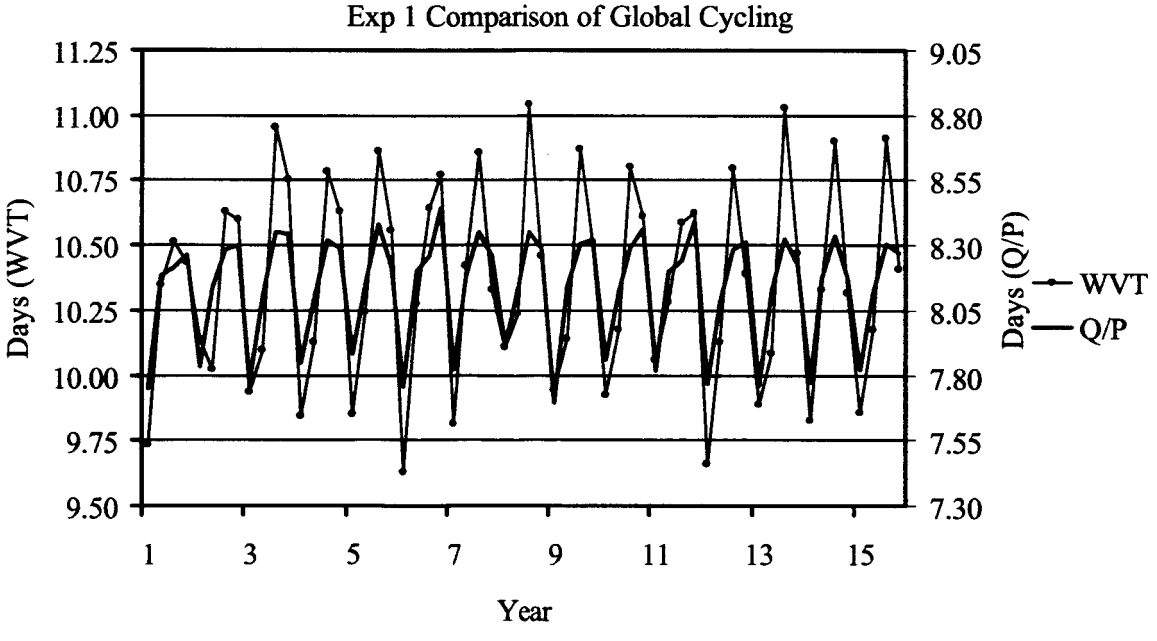

Figure 2 Time series of seasonal residence time ($1/\lambda$) as diagnosed from the WVT method (scale on left axis) and the simple seasonal global average TPW and precipitation (scale on right axis) for 15 years of EXP1 (using late 20th century SST and CO2).

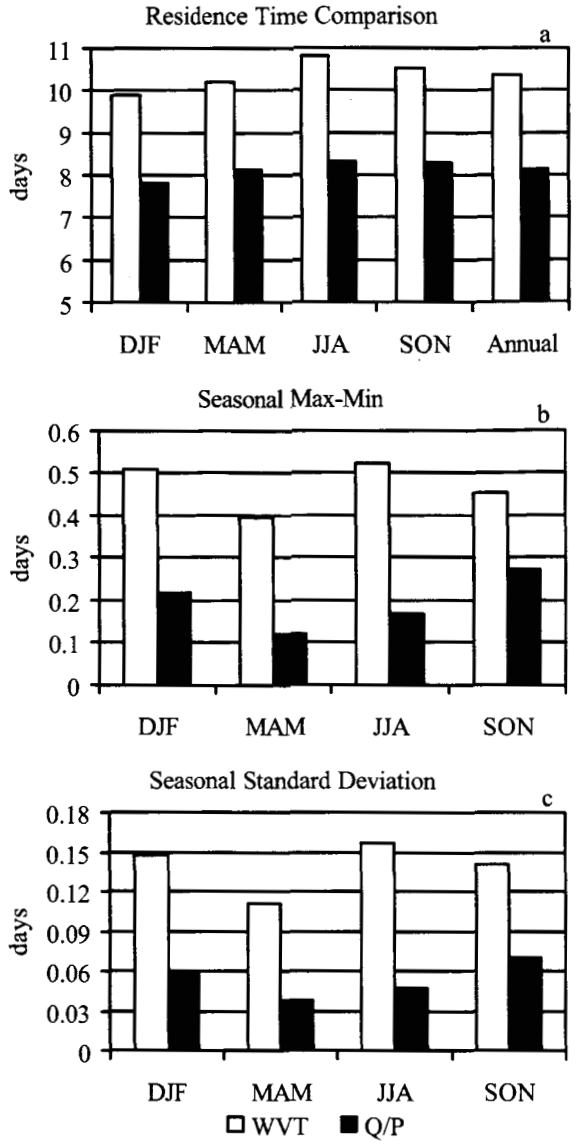

Figure 3 EXP1 seasonal and annual averages of residence time (a), difference of the seasonal maximum and minimum residence time (b), and the standard deviation of the seasonal residence time (c) for the WVT method (white) and simple method (black).

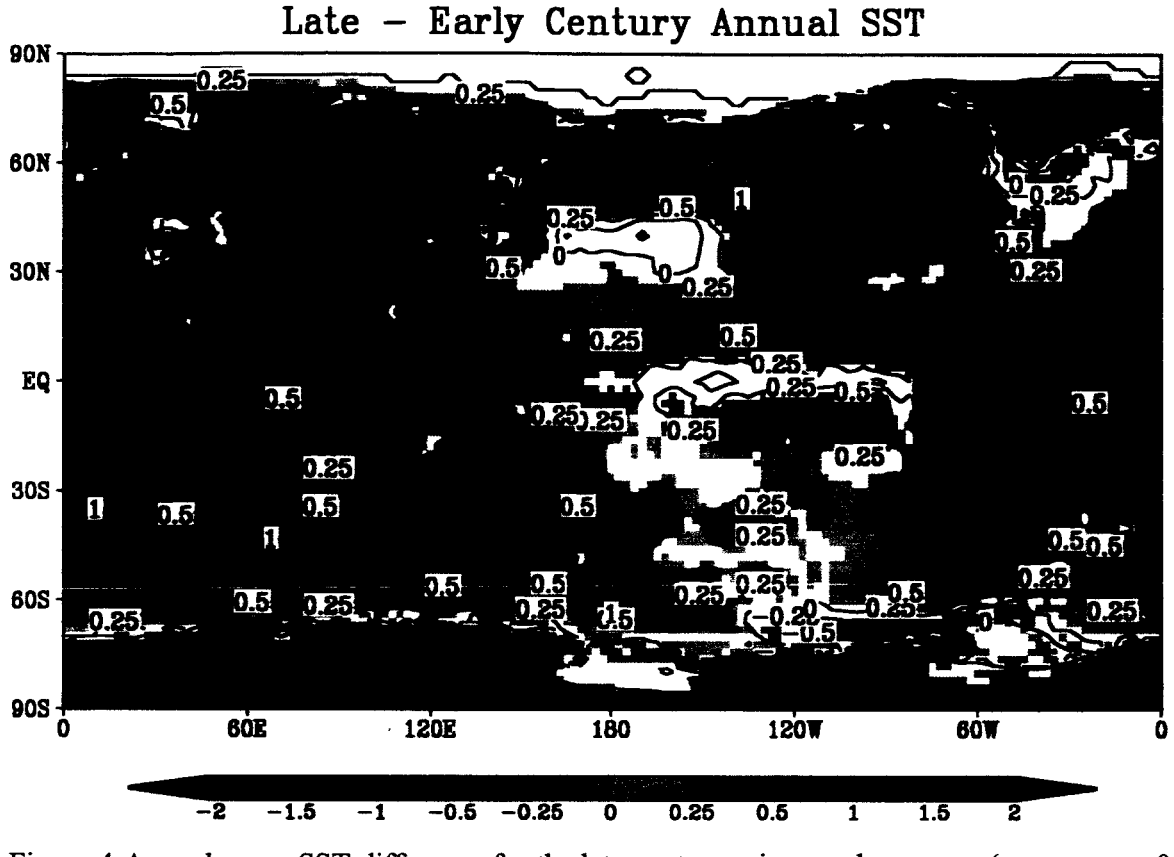

Figure 4 Annual mean SST difference for the late century minus early century (contours at -0.5 -0.2 -0.1 0 0.1 0.2 0.5 1.0 1.5 2.0 Kelvin). Color shaded temperature differences are significant at the 5% level based on a t-test.

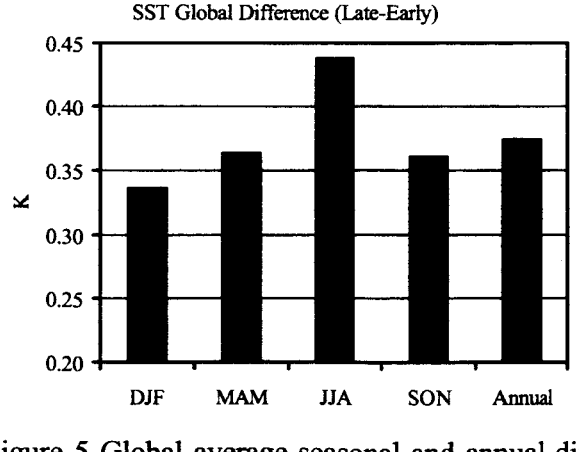

Figure 5 Global average seasonal and annual difference of late century minus early century SST (Kelvin).

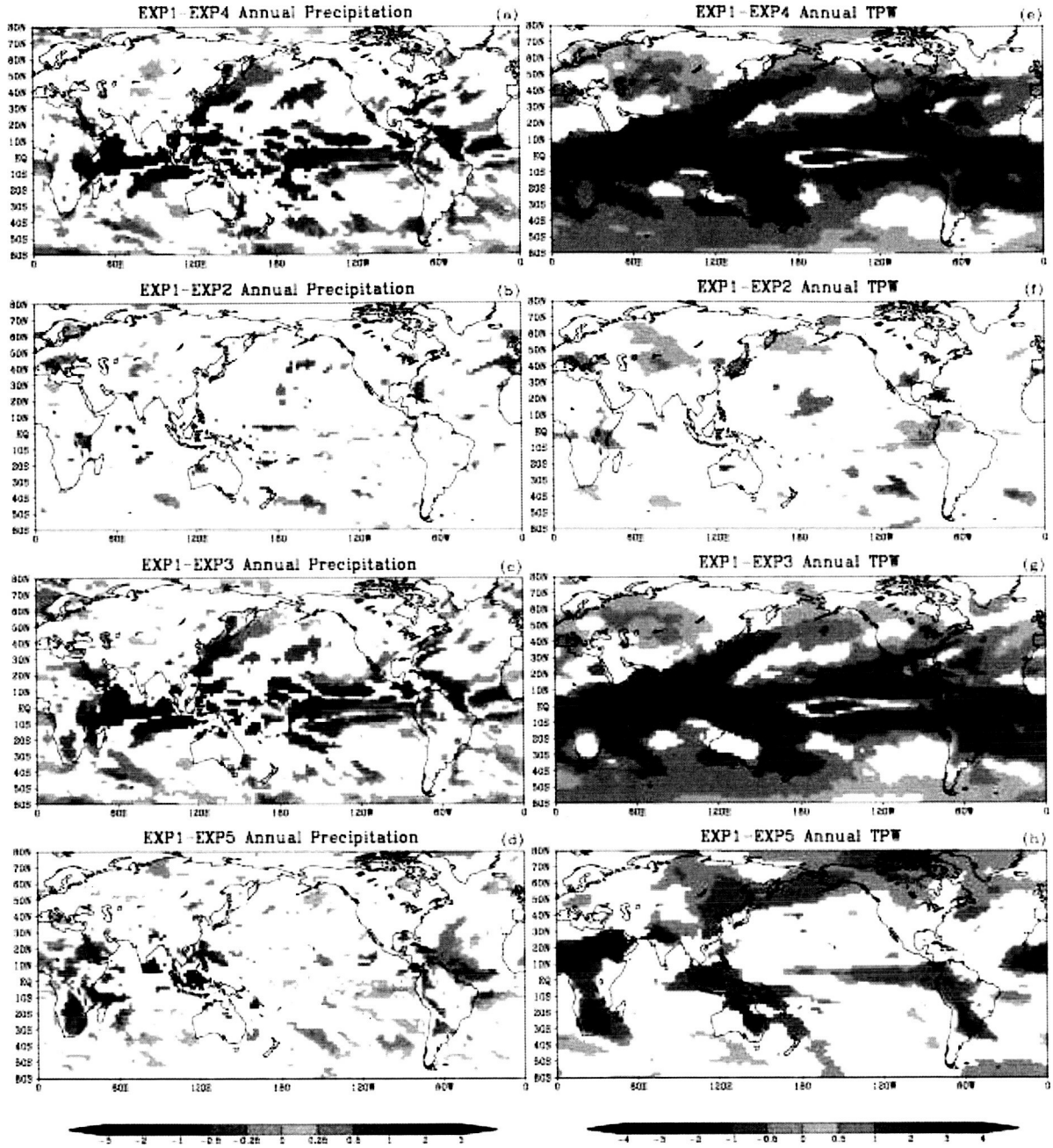

Figure 6 Mean difference of EXP1 precipitation and TPW with each of the other experiments. Only values significant at the 5% level of the t-test between each experiment are plotted.

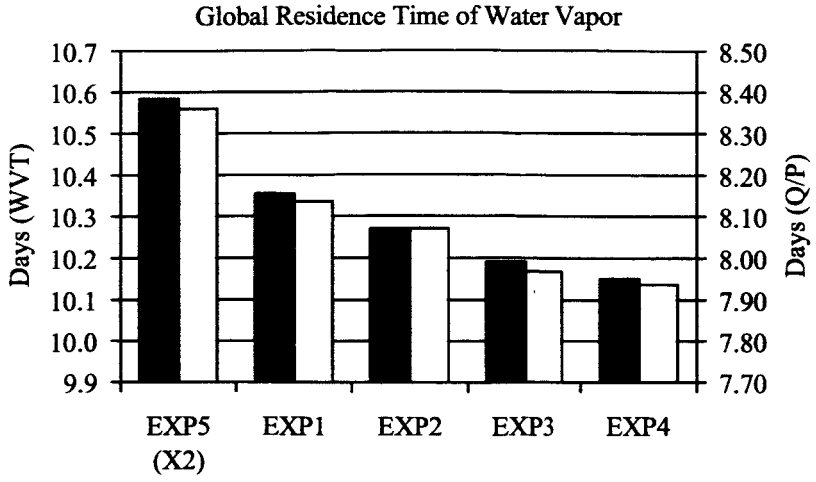

Figure 7 15-year average global mean residence time computed from WVTs (black bar, left axis) and the simple mean Q/P calculation (white bar, right axis).

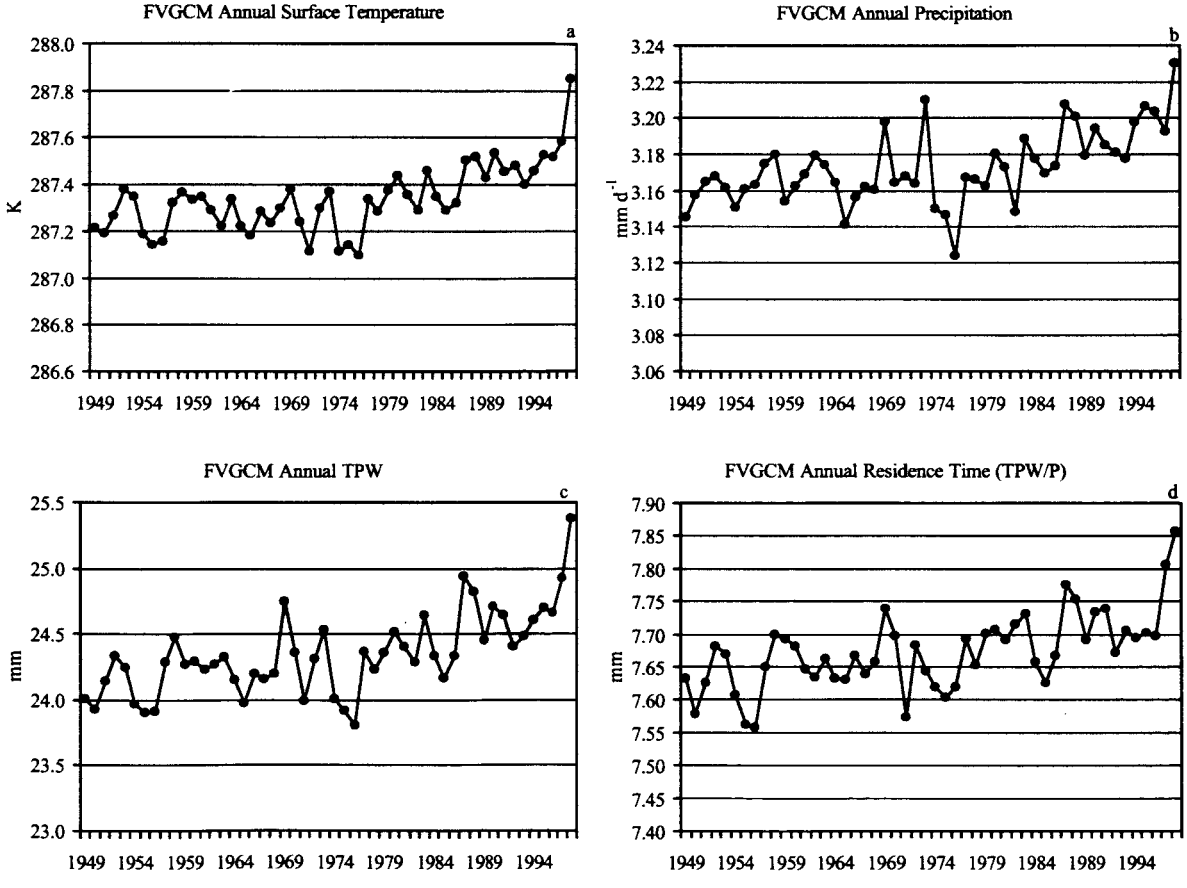

Figure 8 FVGCM global and annual averaged (a) surface temperature, (b) precipitation, (c) total precipitable water, and (d) residence time (computed from the annual means of precipitations and TPW).

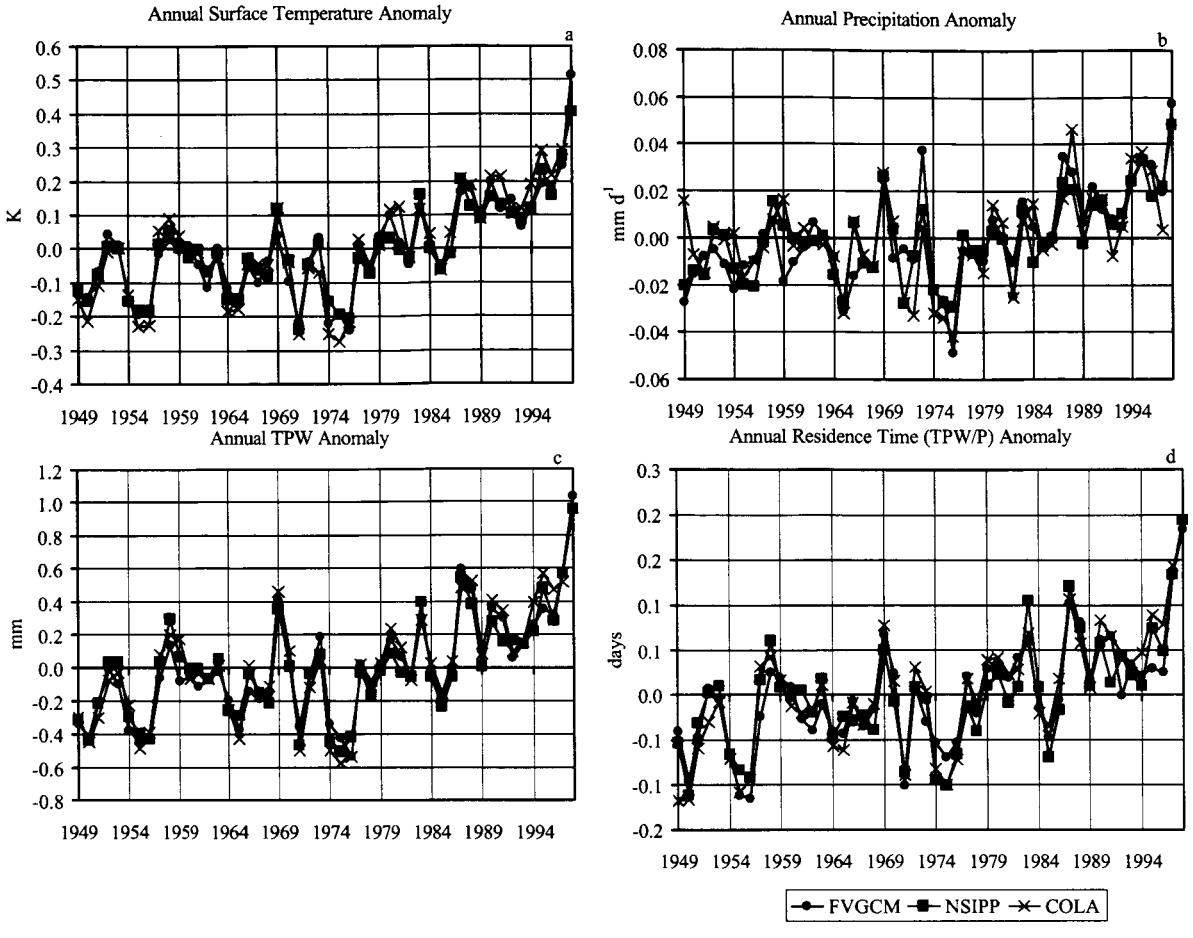

Figure 9 Global and annual average anomalies from long term means for (a) surface temperature, (b) precipitation, (c) total precipitable water, and (d) residence time.

a

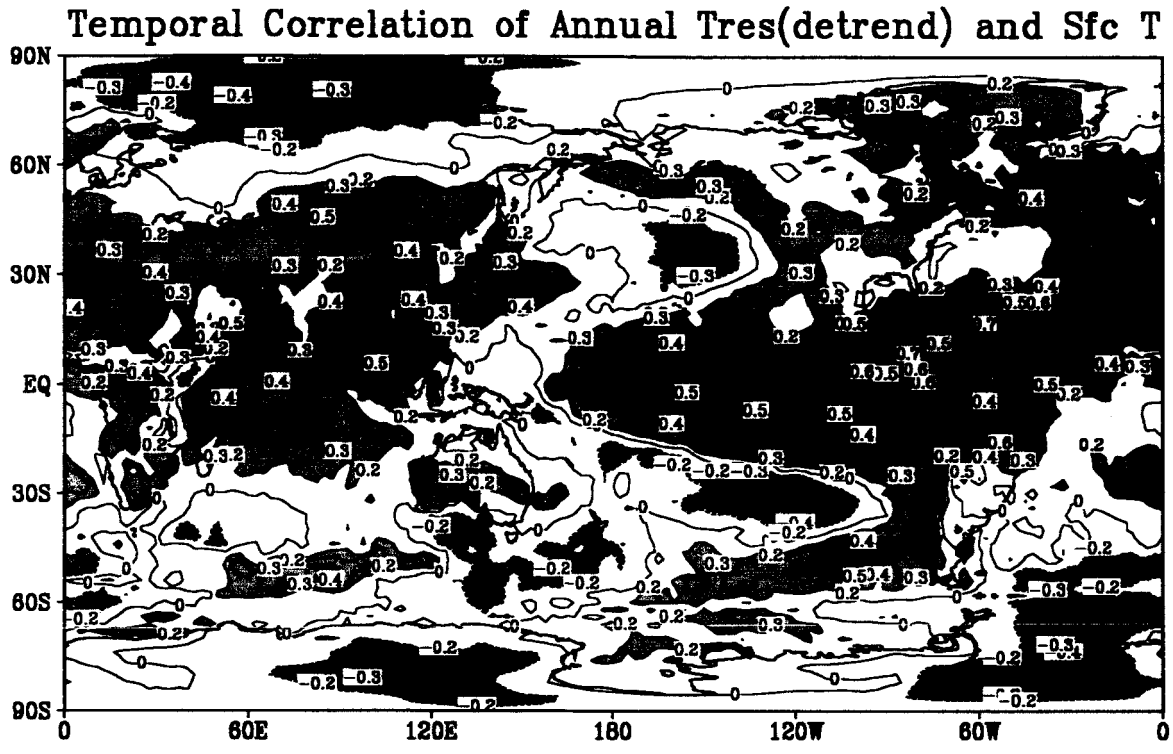
Temporal Correlation of Annual Tres(detrend) and Sfc T
90N
60N
30N
EQ
30S
60S
90S
0
60E
120E
180
120W
60W
0

b

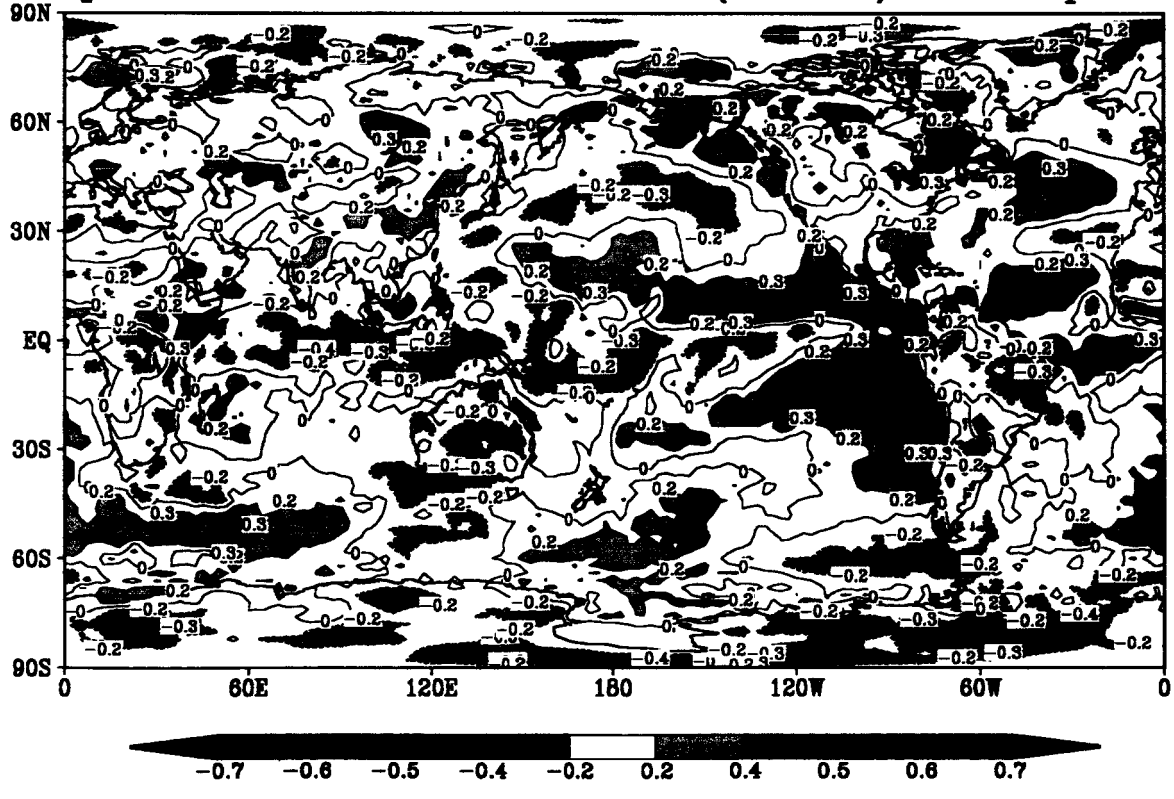
Temporal Correlation of Annual Tres(detrend) and Evaporatior
90N
60N
30N
EQ
30S
60S
90S
0
60E
120E
180
120W
60W
0
-0.7
-0.6
-0.5
-0.4
-0.2
0.2
0.4
0.5
0.6
0.7

Figure 10

c

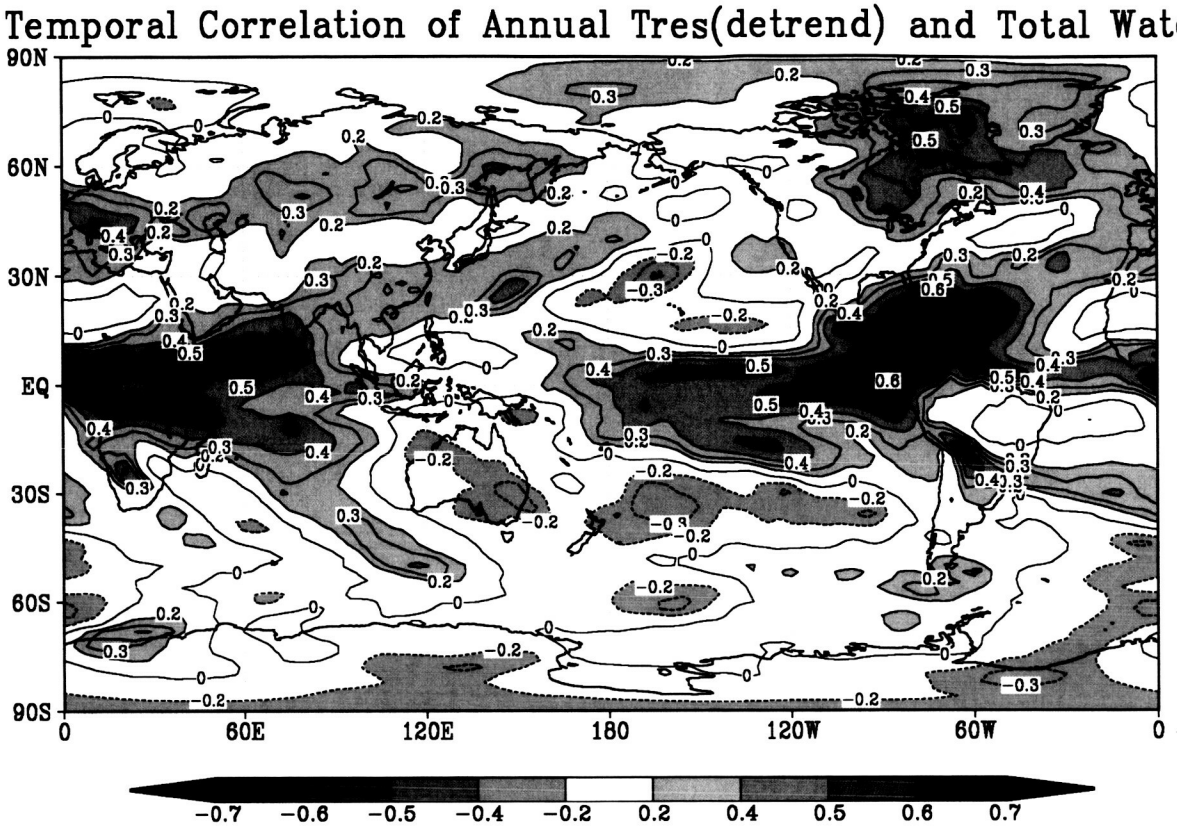

Figure 10 Map of the temporal correlation between the FVGCM detrended time series of annual residence time (as in Figure 9) and annual FVGCM (a) surface temperature (b) evaporation and (c) total precipitable water.

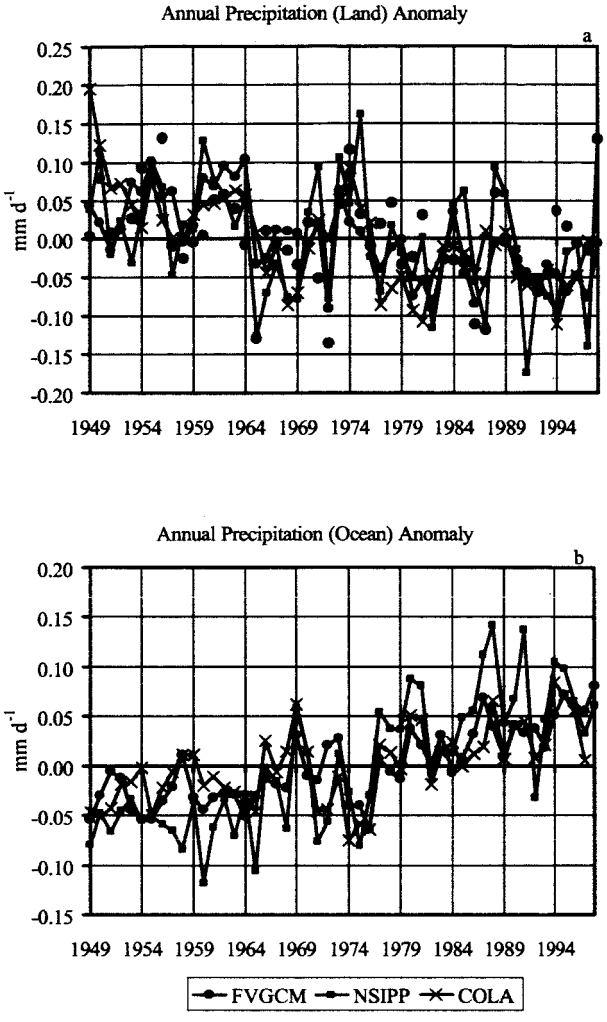

Figure 11 Annual average anomalies from long-term means for (a) precipitation at global land grid points and (b) precipitation at global ocean gridpoints (including the Antarctic continent). The green dots are the global land averaged GHCN gage precipitation data.

(a)

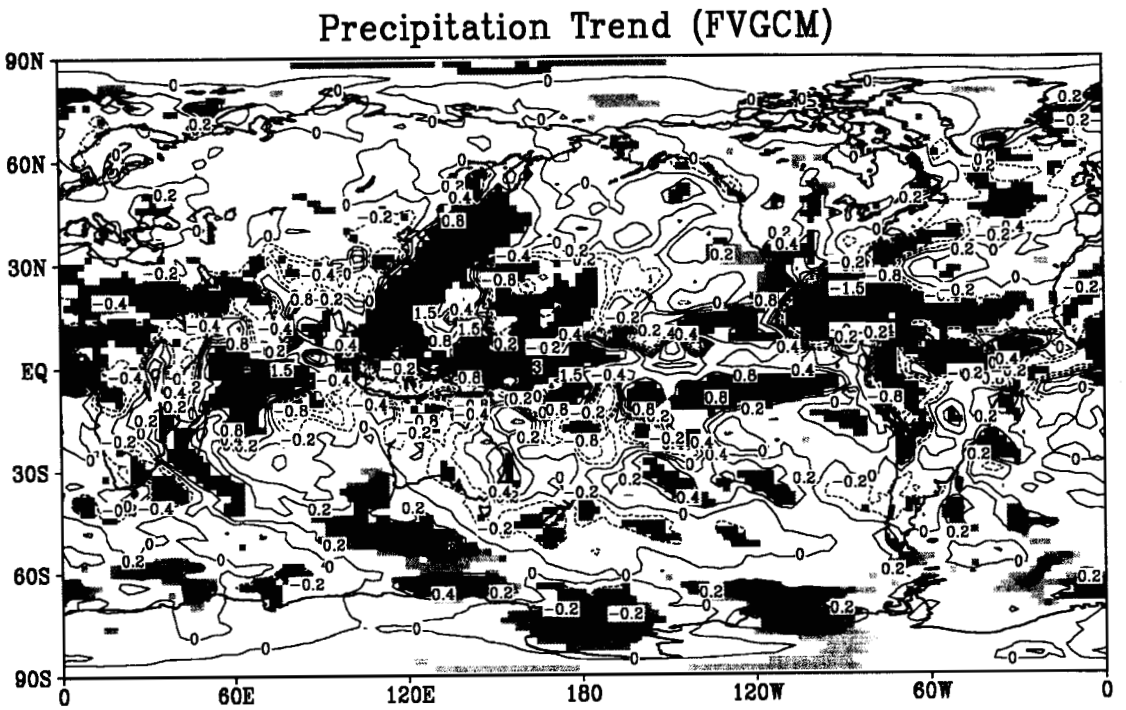
Precipitation Trend (FVGCM)
90N
60N
30N
EQ
30S
60S
90S
0
60E
120E
180
120W
60W
0

(b)

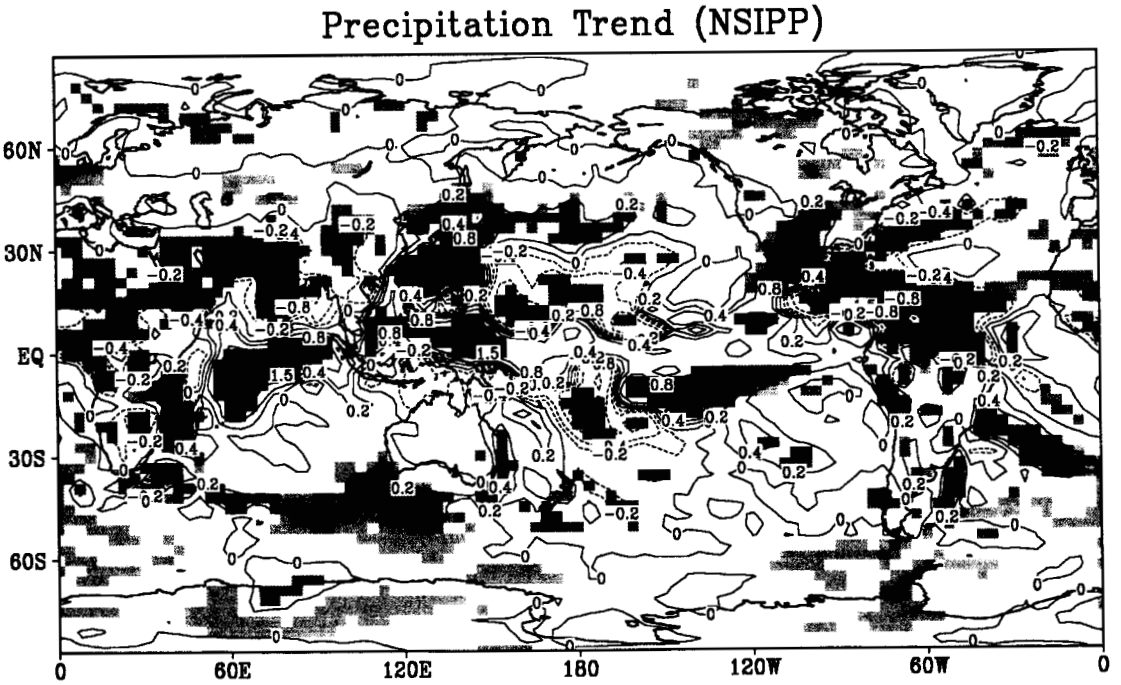
Precipitation Trend (NSIPP)
60N
30N
EQ
30S
60S
0
60E
120E
180
120W
60W
0

Figure 12

(c)

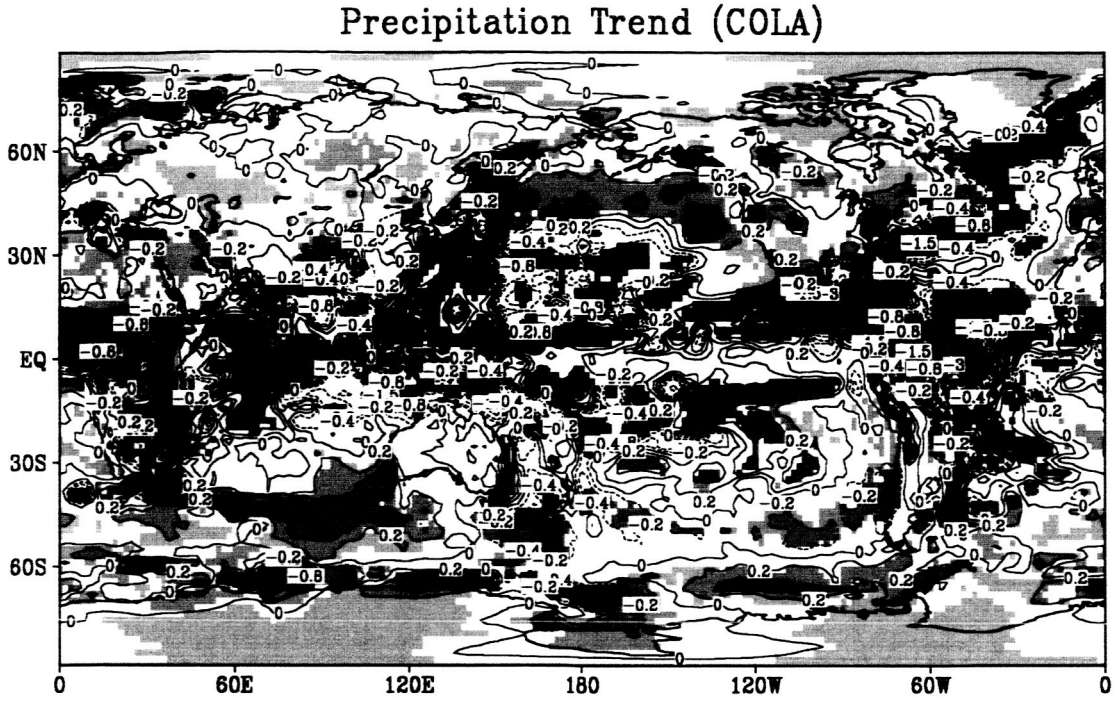

(d)

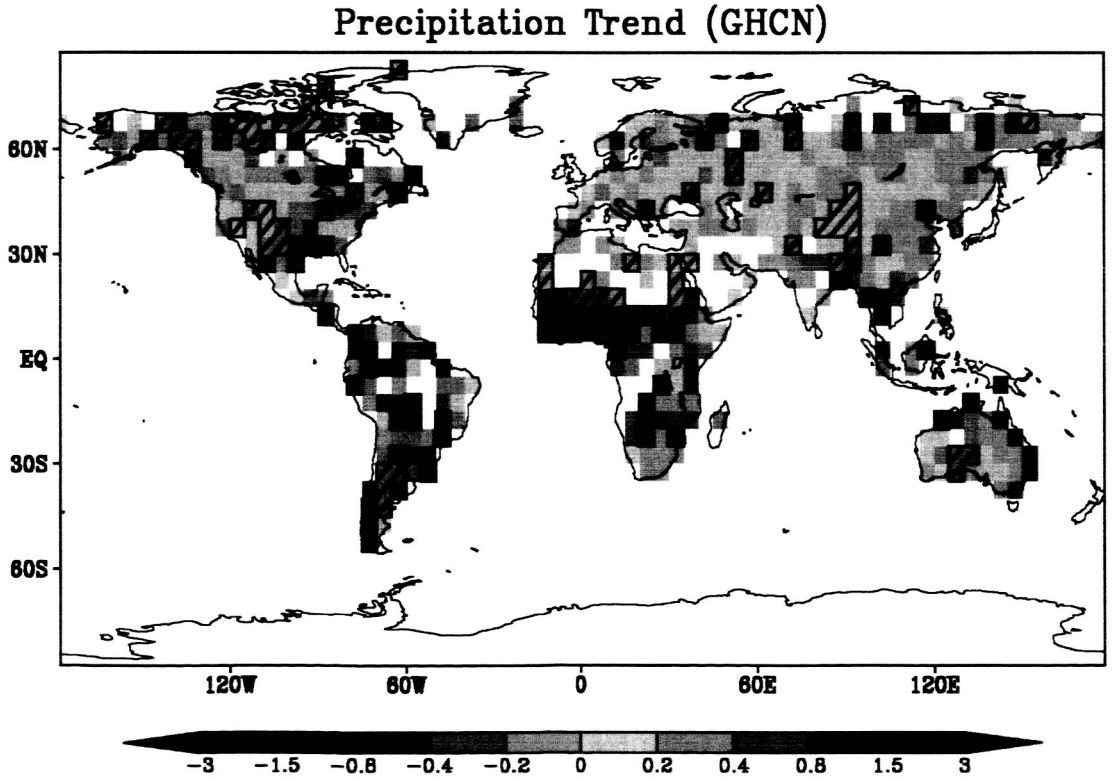

Figure 12 Map of precipitation trends at model gridpoints for (a) FVGCM, (b) NSIPP (c) COLA GCMs and (d) GHCN gage data. The units are mm day-1 per 50 years. For the GCMs, trends significant at 5% from t-tests are color shaded, and all values are contoured in black. The 5% significant trends in the GHCN observations are denoted by crosshatched boxes.

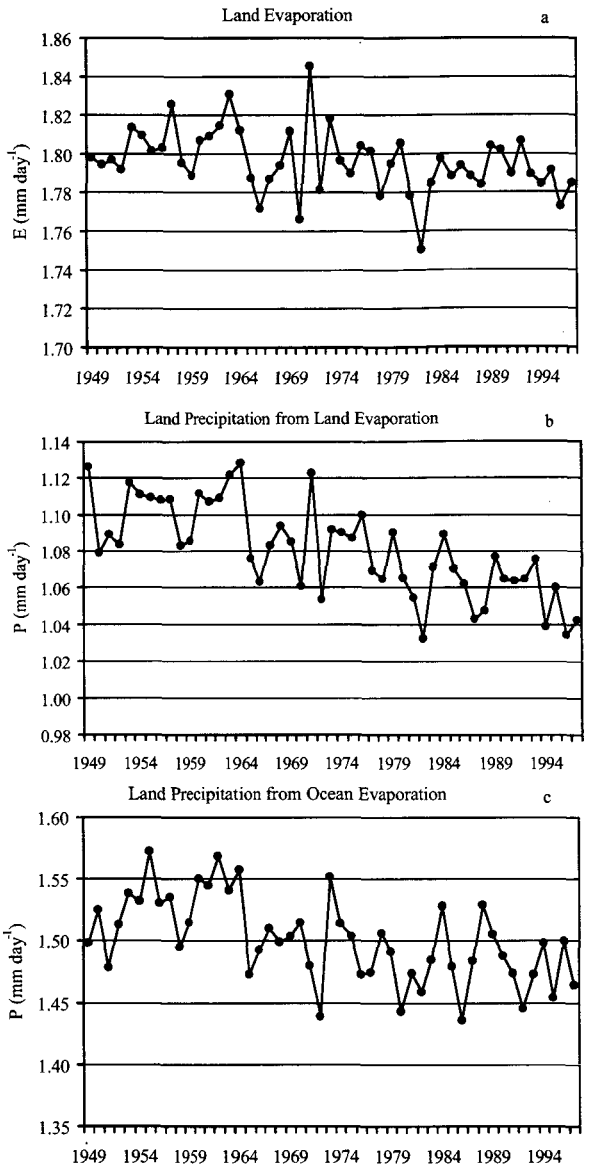

Figure 13 Annual averages of land grid point (a) evaporation, (b) precipitation that occurs from land evaporation and (c) precipitation that occurs from oceanic evaporation (not including the Antarctica continent in the spatial average).

(a)

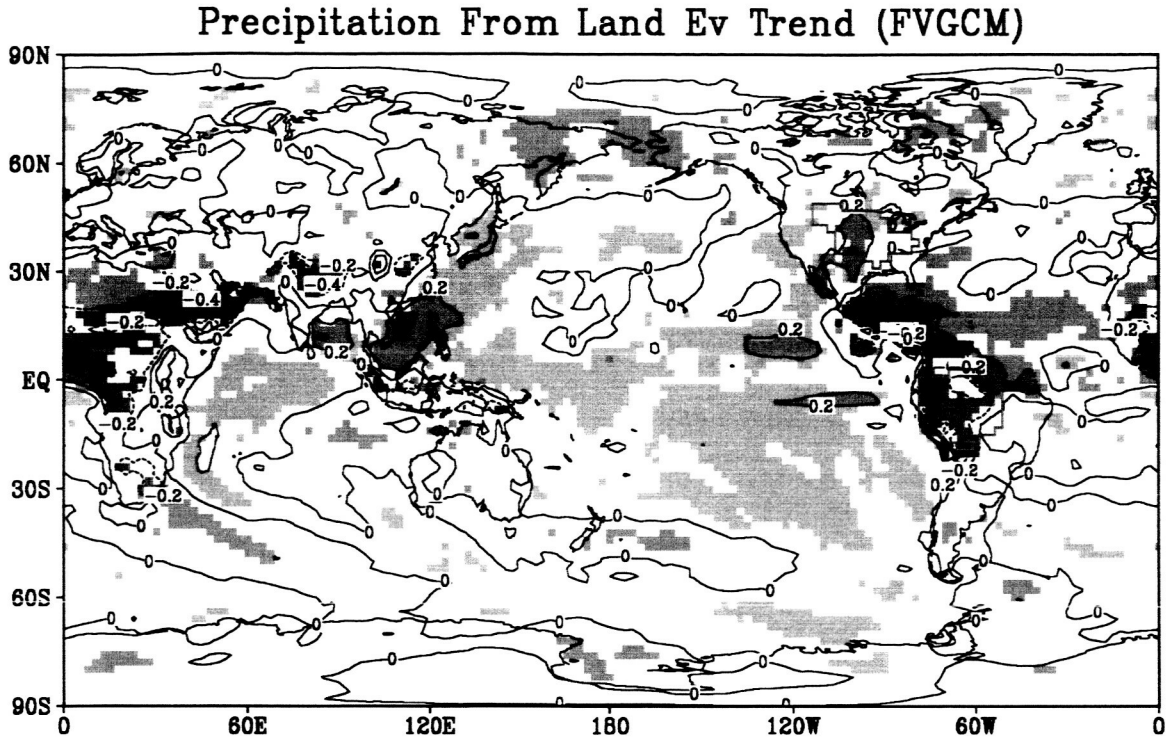
Precipitation From Land Ev Trend (FVGCM)
90N
60N
30N
EQ
30S
60S
90S
0
60E
120E
180
120W
60W
0

(b)

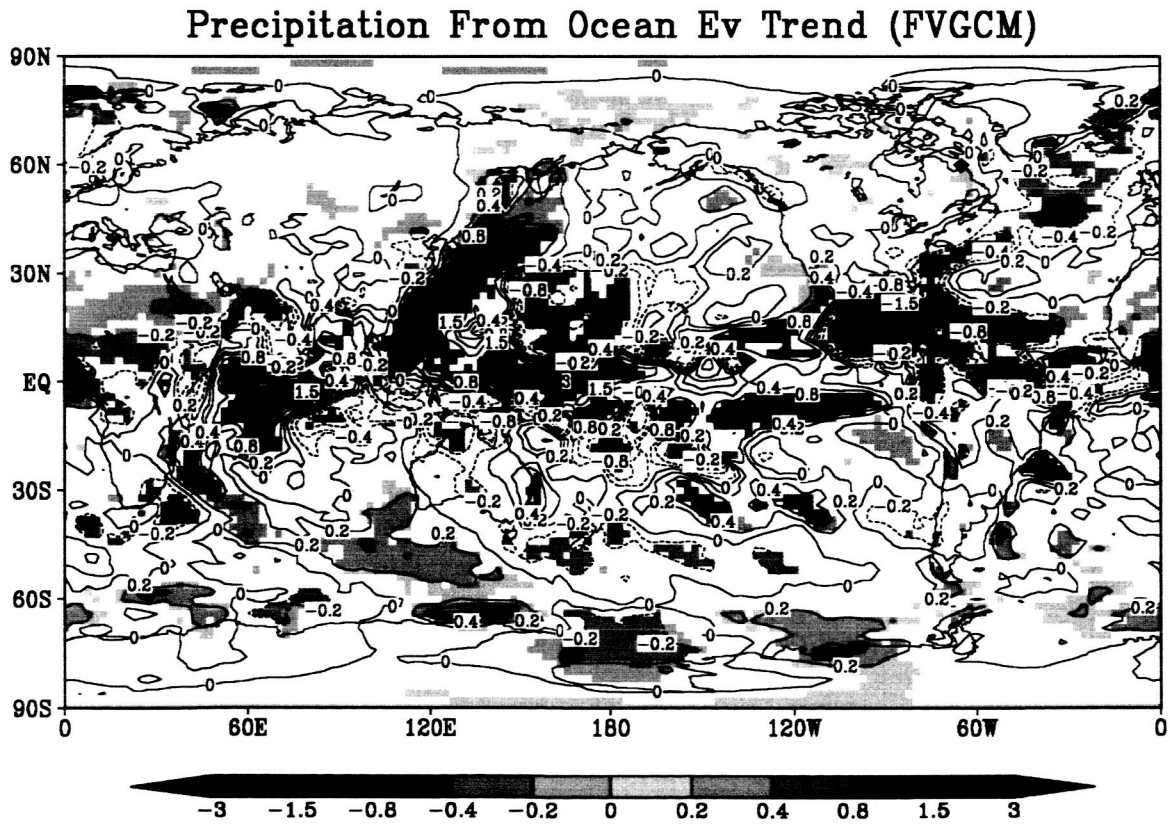
Precipitation From Ocean Ev Trend (FVGCM)
90N
60N
30N
EQ
30S
60S
90S
0
60E
120E
180
120W
60W
0
-3
-1.5
-0.8
-0.4
-0.2
0
0.2
0.4
0.8
1.5
3

Figure 14

(c)

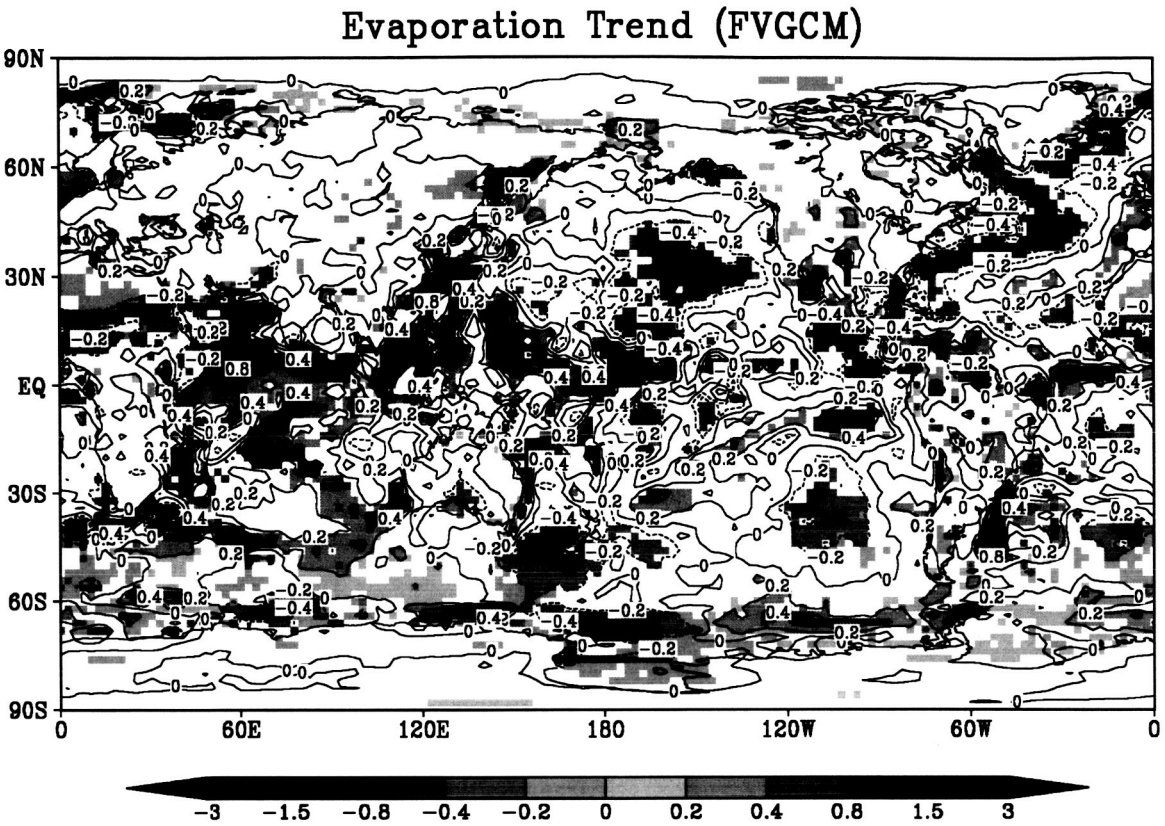

Figure 14 Map of trends at model gridpoints for the FVGCM (a) precipitation that has a continental evaporative source, (b) precipitation that has an oceanic evaporative source and (c) surface evaporation. The regions in (a) outlined in green denote the areas for Mississippi River and Amazon River basin averages.